
























## Probing the IMF in the Early Universe – Direct measurements in the Boötes I UFD with JWST/NIRCam

KEYI DING (丁可悒) <sup>1</sup>, MARIO GENNARO <sup>2</sup>, ROBERTO J. AVILA <sup>2</sup>, MASSIMO RICOTTI <sup>1</sup>, RACHAEL L. BEATON <sup>2</sup>,  
MARTHA L. BOYER <sup>2</sup>, THOMAS M. BROWN <sup>2</sup>, ANNALISA CALAMIDA <sup>2</sup>, SANTI CASSISI <sup>3,4</sup>, VEDANT CHANDRA <sup>5</sup>,  
ROGER E. COHEN <sup>6,7</sup>, MATTEO CORRENTI <sup>8,9</sup>, DENIJA CRNOJEVIĆ <sup>10</sup>, KAREEM EL-BADRY <sup>11</sup>, MARLA GEHA <sup>12</sup>,  
PURAGRA GUHATHAKURTA <sup>13</sup>, NITYA KALLIVAYALIL <sup>14</sup>, EVAN N. KIRBY <sup>15</sup>, KRISTEN. B. W. MCQUINN <sup>2,16</sup>,  
ALESSANDRO SAVINO <sup>17</sup>, CHEYANNE SHARIAT <sup>11</sup>, JOSHUA D. SIMON <sup>18</sup> AND DANIEL R. WEISZ <sup>17</sup>

<sup>1</sup>Department of Astronomy, University of Maryland, College Park, MD 20742, USA

<sup>2</sup>Space Telescope Science Institute, 3700 San Martin Drive, Baltimore, MD 21218, USA

<sup>3</sup>INAF Osservatorio Astronomico di Abruzzo, via M. Maggini snc, I-64100 Teramo, Italy

<sup>4</sup>INFN Sezione di Pisa, Universita' di Pisa, Largo Pontecorvo 3, 56127 Pisa, Italy

<sup>5</sup>Center for Astrophysics | Harvard & Smithsonian, 60 Garden St, Cambridge, MA 02138, USA

<sup>6</sup>Eureka Scientific, 2452 Delmer St., Suite 100, Oakland, CA 94602, USA

<sup>7</sup>Department of Physics and Astronomy, Rutgers the State University of New Jersey, 136 Frelinghuysen Rd., Piscataway, NJ, 08854, USA

<sup>8</sup>INAF Osservatorio Astronomico di Roma, Via Frascati 33, 00078, Monteporzio Catone, Rome, Italy

<sup>9</sup>ASI-Space Science Data Center, Via del Politecnico, I-00133, Rome, Italy

<sup>10</sup>Department of Physics & Astronomy, University of Tampa, 401 West Kennedy Boulevard, Tampa, FL 33606, USA

<sup>11</sup>Department of Astronomy, California Institute of Technology, 1200 East California Boulevard, Pasadena, CA 91125, USA

<sup>12</sup>Department of Astronomy, Yale University, New Haven, CT 06520, USA

<sup>13</sup>Department of Astronomy & Astrophysics, University of California Santa Cruz, 1156 High Street, Santa Cruz, CA 95064, USA

<sup>14</sup>Department of Astronomy, University of Virginia, 530 McCormick Road, Charlottesville, VA 22904, USA

<sup>15</sup>University of Notre Dame, Department of Physics & Astronomy, 225 Nieuwland Science Hall, Notre Dame, IN 46556

<sup>16</sup>Rutgers University, Department of Physics and Astronomy, 136 Frelinghuysen Road, Piscataway, NJ 08854, USA

<sup>17</sup>Department of Astronomy, University of California, Berkeley, Berkeley, CA 94720, USA

<sup>18</sup>Observatories of the Carnegie Institution for Science, 813 Santa Barbara Street, Pasadena, CA 91101, USA

### ABSTRACT

The dependence of the stellar initial mass function (IMF) on star-formation environment, particularly at low metallicities and high redshifts, remains poorly constrained. Ultra-faint dwarf galaxies (UFDs) are local fossils of high-redshift galaxies hosting old, metal-poor populations, and their resolved stellar populations provide unique pathways to constrain the sub-solar IMF. We investigate the low-mass IMF in the Boötes I (Boo I) UFD with JWST/NIRCam, leveraging its capability to resolve over 10,000 stars reaching  $\lesssim 0.15M_{\odot}$ , obtaining one of the largest, deepest resolved stellar samples for UFDs. We explore three different functional forms of the IMF with machine learning and statistical techniques, combining forward modeling of synthetic color-magnitude diagrams with simulation-based inference. We find that a single power-law IMF fails to reproduce the observed luminosity function and also deviates from the canonical Salpeter IMF. Our best-fit broken power-law and lognormal IMF parameters are consistent with the Milky Way within 68% confidence level, providing evidence that star formation at metallicities as low as  $[\text{Fe}/\text{H}] \approx -2.4$  follows a similar IMF as in the Milky Way. By treating Boo I as a local relic analogous to a high-redshift galaxy with a stellar mass of  $\lesssim 10^5 M_{\odot}$  at  $z \gtrsim 6$ , our results provide evidence for the universality of the IMF across both local and high-redshift environments.

**Keywords:** Initial mass function (796) — Stellar astronomy (1583) — Low mass stars (2050) — Dwarf galaxies (416) — Infrared photometry (792)

### 1. INTRODUCTION

The stellar initial mass function (IMF) is an empirical distribution that describes the masses of stars

at birth in a given environment, yet its dependence on the star formation environment—particularly at low metallicities—remains poorly constrained. As a cornerstone of stellar population studies, it connects to many subfields of astrophysics. For instance, on the high-mass end, the IMF determines the number of core-collapse supernovae, gamma-ray bursts, and black hole mergers, setting the expected rate of these energetic events (e.g., [N. C. Weatherford et al. 2021](#)). On the low-mass end, the IMF governs the estimation of galaxies’ stellar masses.

Currently, the nature and variation of the low-mass IMF across different star formation environments are subject to debate both observationally and theoretically, and the physics of turbulence, radiative feedback, and fragmentation within molecular clouds that lead to the IMF remains uncertain. Theoretically, the metallicity determines the major cooling mechanisms and the cooling rate of the protostellar molecular cloud: metal-poor environments are primarily cooled by molecular hydrogen, whereas metal-rich environments are dominated by dust cooling. This shift in cooling physics alters the Jeans mass and, consequently, the shape of the IMF (e.g., [S. Bialy & A. Sternberg 2019](#); [P. Sharda & M. R. Krumholz 2022](#); [R. S. Klessen & S. C. O. Glover 2023](#)). However, some simulations suggest that such variation is weak and difficult to detect (e.g., [A. T. Myers et al. 2011](#); [M. R. Bate 2014, 2019](#); [T. S. Tanvir & M. R. Krumholz 2024](#)), and can be erased by stochastic dynamical effects (see [S. S. R. Offner et al. 2014](#) for a review, and the references therein).

Observationally, [E. E. Salpeter \(1955\)](#) described the Milky Way (MW) IMF as a single power law with a canonical slope of  $\alpha = -2.35$ . These early studies, however, lacked the depth to probe the sub-solar regime, and it has since been observed that the single power-law form diverges toward low masses and does not adequately reproduce the observed MW luminosity function. To address this, low-mass IMF models often incorporate a characteristic break mass, implemented either as a broken power law or a log-normal distribution. Representative examples of these approaches include the IMFs proposed by [P. Kroupa \(2001\)](#) and [G. Chabrier \(2003\)](#). Given that the stellar lifetimes of the low-mass main-sequence stars are comparable to or much longer than the Hubble time, the low-mass IMF can be directly constrained through star counts of resolved stellar populations.

Before the launch of the Hubble Space Telescope (HST), such resolved studies were limited to environments within the Milky Way, as more distant systems could not be observed at the necessary depth. HST

has since overcome this limitation, allowing extragalactic IMF measurements to be directly compared with those of the MW, and observationally test the theory of IMF’s dependence on star formation environments. With HST imaging, [R. F. G. Wyse et al. \(2002\)](#) determined a single power-law IMF for the Ursa Minor (UMi) dwarf spheroidal galaxy, and found its luminosity function to be indistinguishable from that of MW globular clusters, suggesting a potentially invariant IMF across systems with markedly different dark-matter content. Using HST imaging, [J. S. Kalirai et al. \(2013\)](#) investigated the sub-solar IMF of the Small Magellanic Cloud (SMC) and found a similar single power-law slope of  $\alpha = -1.9$ . However, no peak mass was detected in the luminosity function, making it unclear whether the functional form of the IMF and its overall shape differ in extragalactic star-forming environments. The debate over the existence of a characteristic break mass in the SMC IMF was further complicated by deeper observations with JWST. [M. V. Legnardi et al. \(2025\)](#) found that introducing a break mass was unnecessary when probing the outskirts of the SMC, whereas [R. E. Cohen et al. \(2026\)](#) reported a break mass of  $0.49 M_{\odot}$  in a broken power-law fit.

Ultra-faint dwarf (UFD) galaxies, characterized by their old, metal-poor, and dark-matter-dominated nature, have since become popular targets for constraining the low-mass IMF in extreme environments using deep HST imaging. Theories and cosmological simulations indicate that UFDs may have formed before or during the epoch of reionization, acting as ‘fossil’ records that retain the properties of high-redshift galaxies ([M. S. Bovill & M. Ricotti 2009, 2011](#)); this theory is further supported by deep imaging observations ([T. M. Brown et al. 2014](#)). Additionally, with very high mass-to-light ratios, the two-body relaxation times of UFDs exceed the Hubble time, making these systems collisionless. Therefore, unlike globular clusters of similar total mass, where both the total number of stellar particles as well as their spatial density drive the relaxation time well below the Hubble time, UFDs have negligible mass segregation (e.g., [H. Baumgardt et al. 2022](#)), and therefore their stellar mass distributions are not altered by dynamical effects. [M. Geha et al. \(2013\)](#) probed the IMF of Hercules and Leo IV with HST/Advanced Camera for Surveys (ACS) down to  $\sim 0.5 M_{\odot}$  and found single power-law slopes shallower than the [E. E. Salpeter \(1955\)](#) IMF. [M. Gennaro et al. \(2018a\)](#) reanalyzed the [M. Geha et al. \(2013\)](#) data, and extended the sample with four additional UFDs observed with HST/ACS; the analysis probed slightly lower mass ( $0.45 M_{\text{sun}}$ ), and found a mild trend of shallower IMF slope with lower

metallicity. M. Safarzadeh et al. (2022) analyzed the HST/ACS data of Reticulum II for the purpose of detecting wide binaries, and found that a shallower power-law  $1.01 \leq \alpha \leq 1.15$  is necessary to explain the mass function. Nonetheless, neither analysis statistically rejects the MW IMF among all their samples. However, in all these studies, the observations were not deep enough to reach the canonical characteristic mass of the MW IMF at  $\sim 0.2 M_{\odot}$ , and thus, it remained ambiguous whether a single power-law could describe the luminosity function when extrapolating to lower masses. To overcome the lower mass limitation, multiple studies (M. Gennaro et al. 2018b; C. Filion et al. 2022, 2024) analyzed deeper HST data of four UFDs down to  $\sim 0.2 M_{\odot}$ . M. Gennaro et al. (2018b) used WFC3/IR to study Coma Berenices, reaching very low masses in principle, but contamination by background galaxies limited the effective depth. C. Filion et al. (2022) targeted Boötes I (Boo I), a more massive and distant UFD, reaching  $\sim 0.3 M_{\odot}$ , while C. Filion et al. (2024) focused on Reticulum II, Ursa Major II, Triangulum II, and Segue 1 with similar depth. While these studies inferred shallower single power-law slopes, the best-fit broken power-law and lognormal parameters remain consistent with those of the MW within  $\sim 3\sigma$ , albeit with large uncertainties. The small sample size of resolved stars limits the precision with which the low-mass IMF can be constrained. Meanwhile, simulations of the IMF further suggest that fitting a single power-law to an underlying lognormal IMF naturally produces shallower slopes as the lower-mass limit decreases (K. El-Badry et al. 2017), which may explain the range of single power-law slopes reported in studies probing different mass ranges. These limitations illustrate that precisely constraining the low-mass IMF requires both a sufficiently massive UFD and the resolution to reach the canonical MW Chabrier characteristic mass at  $\sim 0.2 M_{\odot}$ .

Boo I is a satellite galaxy of the MW first discovered in the Sloan Digital Sky Survey (V. Belokurov et al. 2006). Spectroscopic studies indicate that it is a dark matter-dominated system, with a mass-to-light ratio of  $165 \pm 45$  (M. Geha et al. 2026), a characteristic of UFDs. It hosts predominantly metal-poor stellar populations with a mean metallicity of  $[\text{Fe}/\text{H}] = -2.4 \pm 0.05$  (M. Geha et al. 2026; N. R. Sandford et al. 2026) and exhibits the relatively simple chemical enrichment history (A. Frebel et al. 2016; N. R. Sandford et al. 2026). Boo I can be considered a “true fossil” of high-redshift galaxies (M. Ricotti & N. Y. Gnedin 2005), with its star formation largely quenched by reionization (T. M. Brown et al. 2014). The finding that nearly 90% of its stars formed before its first infall into the Milky Way (M. Rocha et al.

2012; T. M. Brown et al. 2014; D. R. Weisz et al. 2015; M. J. Durbin et al. 2025) further supports its status as a relic of the high-redshift universe that has experienced little contamination from subsequent star formations. Its proximity to the MW ( $d = 65$  kpc; S. Okamoto et al. 2012) and relatively higher luminosity among UFDs ( $M_V \sim -6.3$  mag) also make it easier to obtain large samples of resolved stars on the low-mass end with deep imaging. Both M. Gennaro et al. (2018a) and C. Filion et al. (2022) used HST/ACS imaging (of different depths) to find the IMF of Boo I to be consistent with that of the MW; however, the uncertainties of the IMF parameters in these studies were jointly driven by observational depth, limited sample size, and foreground/background contamination. To overcome these limitations, we exploit the resolving capability of the JWST Near Infrared Camera (NIRCam) to obtain deep imaging of Boo I reaching  $\lesssim 0.15 M_{\odot}$  and resolve  $\sim 10,000$  member stars, enabling a more robust measurement of the IMF.

The paper is organized as follows: Section 2 describes our observation strategy, source extraction, and artificial star tests. We detail our method to construct stellar models used in subsequent analysis in Section 3, and our method for fitting IMF models to our observations in Section 4. Our results of various models are summarized in Section 5, and we discuss our results in comparison to previous works in Section 6. Our conclusions are summarized in Section 7.

## 2. DATA

### 2.1. Observation and Image Calibration

The target fields were selected to overlap with the HST/ACS imaging of Boötes I (GO-12549; PI: Brown) used in T. M. Brown et al. (2014). Figure 1 shows a Digitized Sky Survey image with the ACS and JWST footprints. We chose filter F150W on the short-wavelength (SW) channel and filter F322W2 on the long-wavelength (LW) channel. These 2 filters offer high sensitivity and provide a color baseline that enables a clear separation of member stars from background galaxies in the color-magnitude diagram (CMD).

The JWST/NIRCam observing setup, including mosaic parameters, dither pattern, and exposure times, is summarized in Table 1. The data were processed using the `jwst` pipeline version 1.17.1 and calibrated using Calibration Reference Data System (CRDS) `jwst_1322.pmap` reference files, with several steps modified from their default behavior. For the SW channel, we enabled the `clean_flicker_noise` step, which removes  $1/f$  noise; disabled the `suppress_one_group` step, which retains the zeroth images during the ramp fitting stage;

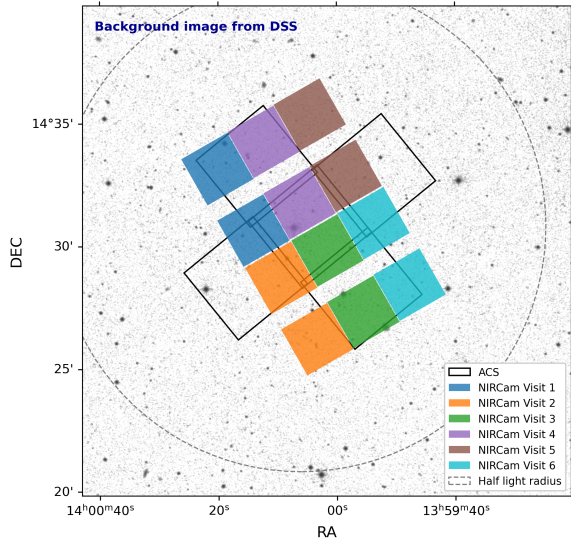


**Figure 1.** Digitized Sky Survey image of Bootes I. The black outlines show the approximate locations of the five ACS visits from [T. M. Brown et al. \(2014\)](#). The solid colored squares show the locations of our F322W JWST observations. Each color corresponds to a visit, and each pair within a colored pair represents the two NIRCcam modules. The dashed circle shows the projected half-light radius based on [R. R. Muñoz et al. \(2018\)](#).

and applied version 3 ([B. Sunnquist et al. 2025](#)) of the Wisp correction algorithm (see the JDOX wisps page<sup>19</sup>), which removes scattered light artifacts from detectors A3, A4, B3, and B4. For the LW images, the only non-default modification to the pipeline was disabling the `suppress_one_group` step.

## 2.2. Photometry

Point-spread function (PSF) fitting photometry was obtained using the DOLPHOT package ([A. E. Dolphin 2000](#); [A. Dolphin 2016](#)) specific to JWST NIRCcam ([D. R. Weisz et al. 2024](#)).

Since the F150W images from the NIRCcam short-wavelength (SW) channel have a higher spatial resolution and depth than the F322W2 images from the long-wavelength (LW) channel, we broke down the photometry run into 3 steps including the adoption of forced photometry in F322W2 using the `warmstart` option for optimal source finding:

- (i) SW Only: for each SW chip, use the `*.i2d` image built from all dithers as the reference frame

<sup>19</sup> <https://jwst-docs.stsci.edu/known-issues/nircam-known-issues/nircam-scattered-light-artifacts#NIRCcamScatteredLightArtifacts-wispsWisps>

Fixed Target	
Name	BOOI
RA (J2000)	14:00:04.0000 (210.0166667°)
Dec (J2000)	+14:30:47.00 (14.51306°)
Mosaic Parameters	
Rows	3
Columns	2
Row Overlap (%)	0.0
Column Overlap (%)	0.0
Row Shift (deg)	0.0
Column Shift (deg)	0.0
Tile Order	DEFAULT
Dither Pattern	
Subpixel Dither Type	STANDARD
Subpixel Positions	20
Spectral Elements	
Short Filter	F150W
Long Filter	F322W2
Readout Pattern	MEDIUM8
Groups/Integration	9
Integrations/Exposure	1
Total Integrations	20
Total Dithers	20
Total Exposure Time (s)	18896.715

**Table 1.** Summary of the JWST observing setup for Boo I.

- (ii) perform source detection and F150W photometry on the individual `*.cal` exposures.
- (iii) SW + LW: feed the source coordinates and signal-to-noise (SNR) from step (ii) into DOLPHOT using the `warmstart` option. This bypasses source detection, forcing DOLPHOT to perform photometry at the given locations for both the F150W and F322W2 bands.
- (iv) Cross-match: cross-match the output catalogs from steps (ii) and (iii) by pixel coordinates, retaining the F150W magnitudes from (ii) and the F322W2 magnitudes from (iii).

We find that using a combined `*.i2d` image from the four SW chips as the reference artificially creates chip-to-chip variations in photometry. We therefore perform photometry on a per-SW-chip basis to mitigate this effect. In our setup, which consists of six non-overlapping mosaic tiles, each with two modules per pointing and four SW chips per module, we divide the photometry run into 48 individual sub-tasks.

The photometry was performed using the VEGA-sirius zero-points<sup>20</sup>, and the DOLPHOT parameters were determined based on recommendations from the JWST Resolved Stellar Populations Early Release Science Program (D. R. Weisz et al. 2024).

### 2.3. Photometric Quality Selection

To identify point sources in the DOLPHOT output that are likely stellar members of Boo I, we apply quality cuts to filter out extended sources, suboptimal detections, and contaminations based on a set of DOLPHOT quality parameters, including the Object Type, Flag, Sharpness, Crowding, and SNR.

DOLPHOT classifies each detected source with an Object Type: 1) bright star, 2) faint star, 3) elongated source, 4) object too narrow, or 5) extended source. Additionally, it assigns a Quality Flag for each filter, indicating potential issues: 0 (good measurement), 1 (aperture off-chip), 2 (many bad/saturated pixels), 4 (centrally saturated), or 8 (extreme case). Multiple values can be added to the flag if multiple issues occur. The Sharpness (sharp) measures the angular extent of the source in comparison with the PSF full width at half maximum (FWHM), with a large negative value indicating extended sources such as background galaxies. The Crowding parameter (Crowd) quantifies the level of blending by measuring how much brighter a star would be if neighboring sources were not fit simultaneously.

We use the quality cuts from J. T. Warfield et al. (2023) and D. R. Weisz et al. (2024) as the baseline and add tighter cuts to ensure that the data quality satisfies our main purpose of fitting the IMF. Our final quality criteria include:

1.  $\text{ObjectType}_{\text{SW}} \leq 2$  &  $\text{ObjectType}_{\text{LW}} \leq 2$
2.  $\text{Flag}_{\text{F150W}} \leq 2$  &  $\text{Flag}_{\text{F322W2}} \leq 2$
3.  $\text{SNR}_{\text{F150W}} > 12$  &  $\text{SNR}_{\text{F322W2}} > 6$
4.  $\text{Sharp}_{\text{F150W}}^2 \leq 0.01$  &  $\text{Sharp}_{\text{F322W2}}^2 \leq 0.01$
5.  $\text{Crowd}_{\text{F150W}} \leq 0.25$  &  $\text{Crowd}_{\text{F322W2}} \leq 0.5$
6. we empirically fit a curve of  $\log(\frac{1}{\text{SNR}})$  as a function of magnitude for each band, and reject sources if the difference between the extracted and fitted  $\log(\frac{1}{\text{SNR}})$  is greater than 0.2 (Appendix A)

The left panel of Figure 2 shows the 12,889 point sources that passed our quality cuts, overlaid on the

full sample of 1,376,174 detected sources. This selected sample, however, still contains some contamination from foreground stars and unresolved background galaxies. Specifically, there is a group of unresolved galaxies with  $\text{F150W} - \text{F322W2} > 0.8$  and a vertical band of foreground stars at  $\text{F150W} - \text{F322W2} \approx 0.6$ .

### 2.4. Member Stars Identification

One advantage of using the SW+LW channels of JWST NIRCcam is that they provide a color baseline that substantially reduces contamination from background galaxies, and the F150W+F322W2 filter combination was specifically chosen for this program to maximize color separation. Following a similar method used in M. Gennaro et al. (2018b), we derived the best-fitting spectral template from photometry of HUDF galaxies using the methodology of C. Pacifici et al. (2012, 2013). These templates, which model galaxy mass, star formation history, and redshift, were then used to calculate synthetic magnitudes in the NIRCcam passbands. As the middle panel of Figure 2 shows, HUDF galaxies are almost exclusively redder than the Boo I main sequence, aligning with the contaminated sources in our sample. When the HUDF galaxy count is scaled based on the field-of-view of the HUDF to match our observation, the background contamination is negligible.

To estimate the level of contamination from foreground stars, we use the TRILEGAL model (L. Girardi et al. 2012) to generate a synthetic CMD of the MW stars along the sight of Boo I with an area matching the field-of-view of our observations. The resulting synthetic CMD recovers both the color and density of the vertical band of foreground stars seen in our data. The simulation suggests that at the depth of our observation, the foreground population mostly consists of M-dwarfs and brown dwarfs in the Galactic halo, and they rarely overlap with the main-sequence of Boo I on the CMD.

Our contamination estimate is in good agreement with the prediction shown in Figure 4 of R. E. Cohen et al. (2026), supporting a consistent picture when using the same JWST/NIRCcam filters. We apply color and magnitude cuts to the CMD to select likely Boo I member stars. We also impose an upper magnitude limit of  $\text{F150W} = 21$ , as in the turn-off and giant regimes, a narrow mass bin maps to a broad range in magnitude, which can introduce stochastic biases in the inference depending on the sampled magnitudes. The resulting sample of 11,046 candidate members is plotted in black in the right panel of Figure 2.

### 2.5. Chip-dependent Offset Removal

Although per-chip-level calibration significantly reduces chip-to-chip variations, it does not fully eliminate

<sup>20</sup> <https://jwst-docs.stsci.edu/jwst-near-infrared-camera/nircam-performance/nircam-absolute-flux-calibration-and-zeropoints>

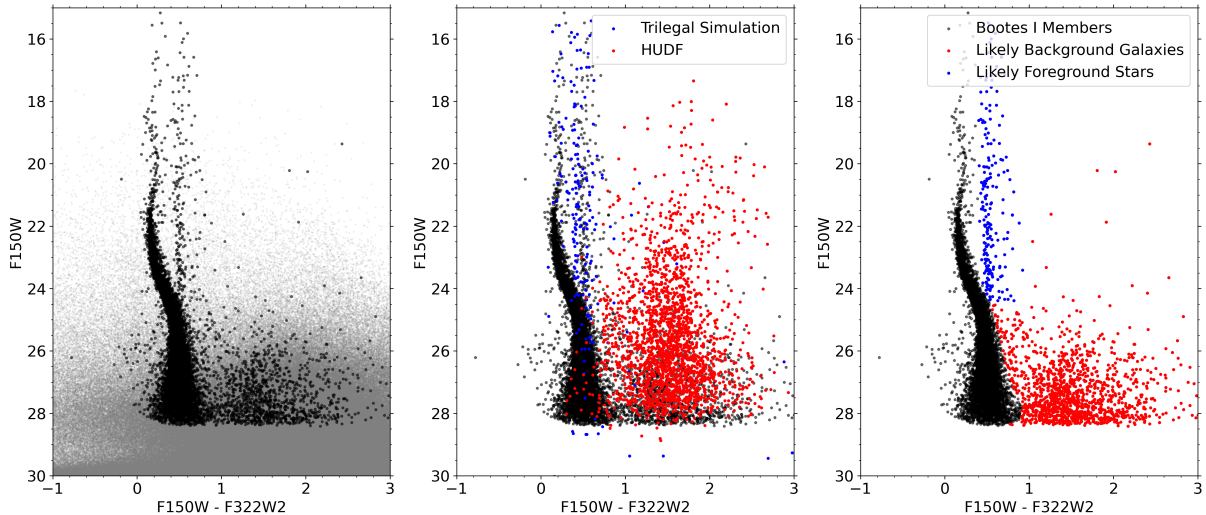


**Figure 2.** CMD of sources extracted by DOLPHOT. Left: All photometric sources are shown in gray, with those passing the data quality cuts highlighted in black. Middle: Sources passing the quality cuts, overplotted with a synthetic foreground stellar population from TRILEGAL (blue) and synthesized photometry of background galaxies from the Hubble Ultra Deep Field (HUDF) based on SED models (red), scaled by area to match the field-of-view of our observations. Right: The final selection of Boo I member stars in black, with likely foreground stars in blue and likely background galaxies in red based on color and magnitude cuts. The Boo I member giants, which we also exclude in our analysis, are plotted in green.

them. We find that these offsets are highly consistent across visits and mosaic tiles, indicating that they are intrinsic to the detector calibration rather than arising from the mosaic construction. To correct for non-negligible photometric offsets among detector chips in JWST/NIRCam, we apply a chip-shift correction to the final catalog after identifying likely Boo I members as described below. For each NIRCam LW module, we divide the stellar catalog into SW chip-specific subsets and select main-sequence stars with  $23 < F150W < 28$  to serve as stable fiducial references for measuring chip-to-chip offsets. For each SW chip, we estimate the mean photometric shift relative to a reference chip (a2 for module A and b3 for module B) using bootstrap resampling, performing 5000 iterations with replacement. The resulting shift (ranging from 0.005 to 0.022 magnitude in F150W) is applied to the F150W magnitude, as SW chips sharing the same LW module are not expected to exhibit chip-dependent offsets in F322W2. We then use the same bootstrap procedure to estimate the color offset between the two LW detectors and apply the corresponding correction to the F322W2 magnitude.

### 2.6. Artificial Star Tests

We conduct artificial star tests (ASTs) to evaluate photometric errors, systematic uncertainties, and completeness. In the ASTs, DOLPHOT injects mock stars with given locations and magnitudes in each band into the images, and attempts to recover the magnitudes along with other photometric parameters using the same

setup as the photometry run. We generate the input magnitudes for the artificial star catalog in two steps. First, we sample 10,000 F150W magnitudes between 20 and 30.5 from a power-law luminosity function with a slope of 2. Next, we derive the corresponding colors by numerically interpolating the main sequence colors of Boo I stars as a function of their F150W magnitude. For each of these 10,000 color-magnitude pairs, we generate 100 realizations by sampling from a Gaussian distribution centered on the interpolated color with a standard deviation of 0.05. This process yields a catalog of 1,000,000 artificial stars. Additionally, we randomly sample another 200,000 stars that uniformly cover the color-magnitude space with  $-0.2 < F150W - F322W2 < 1$  and  $16.5 < F150W < 30.5$ . Given the nearly uniform density profile of Boo I within our observed fields, we assign spatial coordinates to the artificial stars by uniformly distributing them across the field of view. The magnitude catalog is randomly divided into 48 subsets, one for each SW chip. We process the artificial stars following the same warmstart procedure as the photometry. First, we perform AST on the SW images only. Using the recovered positions from this initial run, we then execute a second AST run on the combined SW and LW images. We apply the same data quality flags and chip-dependent shifting to the artificial stars to identify non-detections and bad measurements.

Figure 3 presents the luminosity functions of the input and recovered stars, along with their completeness ratio. The 50% completeness level, marked by red dashed

lines, occurs at  $F150W = 27.9$  and  $F322W2 = 27.3$ . The completeness falls short of 100% even at the bright end because some artificial stars land on image edges or bad pixels and are therefore not detected. The combined input and output CMDs for the ASTs are shown in Appendix B.

### 3. STELLAR MODELS

Using our catalog of Boo I member stars, we overlay the CMD with BaSTI isochrones (A. Pietrinferni et al. 2021) of various ages, adopting  $[\alpha/\text{Fe}] = +0.4$  and  $[\text{Fe}/\text{H}] = -2.4$ , to visually assess the agreement between the data and stellar evolution models. The comparison indicates that the observed CMD exhibits a dimmer turn-off magnitude than predicted by isochrones corresponding to the literature age estimates, and an adequate fit would require an isochrone older than the Hubble time. This discrepancy suggests that a more detailed treatment of chemical abundances is required to reproduce the observed CMD accurately. Observations of metal-poor stars in the MW halo indicate that oxygen abundance increases with decreasing metallicity (A. Frebel 2010), and high  $[\text{O}/\text{Fe}]$  was also detected in the Segue I UFD (T. M. Sitnova et al. 2021). The additional oxygen enhancement primarily affects the rate of the CNO cycle, and consequently, variations in the oxygen abundance can modify the main-sequence lifetime, and thus the turnoff age and luminosity. Based on the calculations of T. M. Brown et al. (2014), increasing  $[\text{O}/\text{Fe}]$  by 0.5 dex would cause the isochrones to appear approximately  $\sim 1$  Gyr younger when inferred from the turnoff luminosity, which aligns with the discrepancy observed between our data and the BaSTI models.

We use the  $\alpha$ -enhanced, O-enhanced models used by T. M. Brown et al. (2014), computed using the Victoria-Regina evolutionary code (D. A. Vandenberg et al. 2014). The models have a metallicity range of  $-4.0 < [\text{Fe}/\text{H}] < -1.0$ , an  $\alpha$ -enhancement of  $[\alpha/\text{Fe}] = +0.4$ , and an additional oxygen enhancement that increases at low  $[\text{Fe}/\text{H}]$  (see Section 3.2 of T. M. Brown et al. 2014 for more details). To transfer the models into JWST bands, we calculate synthetic JWST magnitudes from the Model Atmospheres with a Radiative and Convective Scheme (MARCS; B. Gustafsson et al. 2008) spectra, using the `synphot` Python package (STScI Development Team 2018). While increasing the oxygen abundance can slightly reduce the effective temperature of low-mass stars (D. A. Vandenberg et al. 2022; D. A. Vandenberg 2023) and affect their spectral energy distributions (S. Cassisi & M. Salaris 2020), these effects diminish with decreasing metallicity and are expected to be smaller than the typical observational uncertainties

in the UFD regime. Therefore, we use the  $\alpha$ -enhanced model grid in the MARCS atmospheres without accounting for the oxygen enhancement in the spectral modeling. It must be noted that, to our knowledge, no synthetic stellar spectral library allows for additional O-enhancement with respect to a baseline  $[\alpha/\text{Fe}] = +0.4$ , and thus our choice is not only justified, but in fact a necessity.

The oxygen-enhanced model grid is defined only for stellar masses above  $0.4M_{\odot}$ . For stars below this limit, we recomputed the models using the  $\alpha$ -enhanced BaSTI grid (A. Pietrinferni et al. 2021), extending down to  $0.1M_{\odot}$ . To create a smooth handoff between the BaSTI and oxygen-enhanced models, we gradually blend their magnitudes over the mass range  $0.4M_{\odot}$  to  $0.6M_{\odot}$ . The transition is controlled by a cubic Hermite weight function:

$$w(m) = \frac{(m_{\text{low}} - m)^2 \left[ 3 - 2 \frac{(m_{\text{low}} - m)}{(m_{\text{low}} - m_{\text{high}})} \right]}{(m_{\text{low}} - m_{\text{high}})^2} \quad (1)$$

where  $m_{\text{low}} = 0.4M_{\odot}$ ,  $m_{\text{high}} = 0.6M_{\odot}$ , and  $w(m)$  is a smooth function ranging from 0 to 1, ensuring that both the value and slope of the interpolated magnitudes match at the boundaries. The interpolated magnitude is then

$$\text{mag}(m) = w(m) \times \text{mag}_{\text{O-enhanced}} + [1 - w(m)] \times \text{mag}_{\text{BaSTI}} \quad (2)$$

so that stars below  $0.4M_{\odot}$  follow the BaSTI model, those above  $0.6M_{\odot}$  follow the oxygen-enhanced model, and intermediate masses transition smoothly between the two. Figure 4 shows the comparison between the  $\alpha$ -enhanced O-enhanced isochrones, assuming an extinction  $E(B - V) = 0.0157$  and a distance of 65 kpc. We acknowledge that this interpolation introduces some inaccuracy due to differences in the underlying model and the limited calibration of the metal-poor,  $\alpha$ -enhanced stellar populations, but the resulting magnitude shifts are small compared to the typical photometric uncertainties at the low-mass end.

### 4. METHOD

We have developed `Starwave`<sup>21</sup> (M. Gennaro et al. 2026), a Python-based code that performs Bayesian inference to determine stellar population parameter sets. We keep the core logic of the method used in M. Gennaro et al. (2018a): proposing parameters from a prior, simulating corresponding CMDs, and evaluating them against the observed CMD. However, `Starwave` implements an alternative to the traditional ABC-MCMC

<sup>21</sup> <https://github.com/Resolved-Stellar-Populations/starwave>

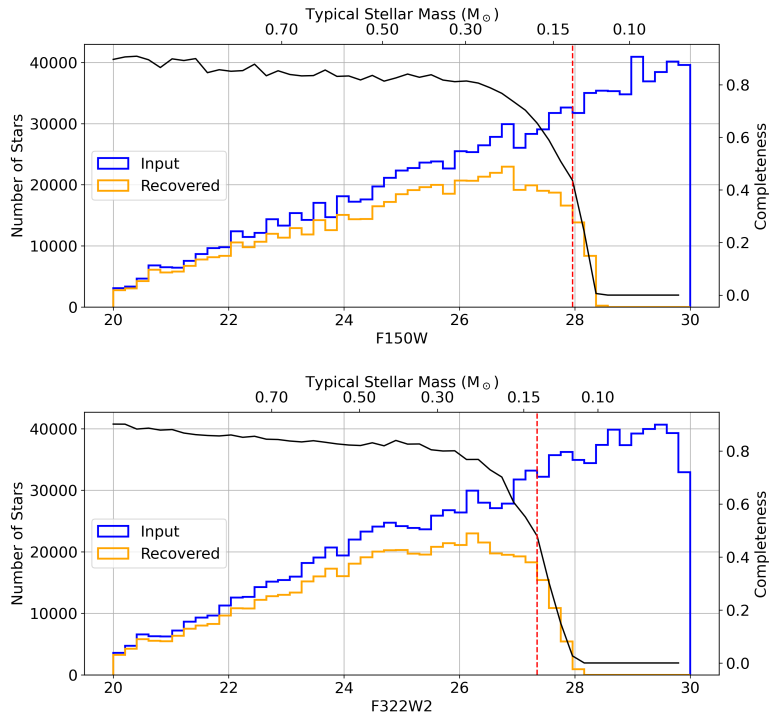


**Figure 3.** Luminosity function of the input magnitudes (blue) and the recovered magnitudes (orange) of the artificial stars in the F150W (top) and F322W2 (bottom) filters. The ratio of these functions (black line) represents the photometric completeness as a function of magnitude. Red vertical dashed lines mark the 50% completeness limits, while the top x-axis displays the corresponding typical stellar masses based on the stellar model.

method in [M. Gennaro et al. \(2018a\)](#). Instead, we employ Simulation-based Inference (SBI; [K. Cranmer et al. 2020](#)), leveraging neural networks to achieve more efficient parameter estimation. (The initial development of *Starwave*, built on the `sbi` Python package ([A. Tejero-Cantero et al. 2020](#)), was presented at the 237th AAS conference by [V. Chandra & M. Gennaro 2021](#))

#### 4.1. Simulating Synthetic CMDs

In the forward modeling process, we use a simulator to generate synthetic CMDs based on a set of stellar populations and IMF parameters. The simulator begins by drawing samples for IMF parameters, binary fraction, star formation history (SFH, includes age and  $[\text{Fe}/\text{H}]$ ), distance modulus, and extinction from provided distributions. With the drawn IMF parameters, we sample a set of individual stellar system masses and randomly assign them stellar ages and  $[\text{Fe}/\text{H}]$  based on the drawn SFH. Then we assign absolute magnitudes to each star by interpolating the grid of stellar isochrones, and convert to apparent magnitudes by adding distance modulus and extinction. Under the assumption that most binary stars are unresolved ([C. Shariat et al. 2025](#)),

we model them by calculating their mass ratio, interpolating individual stellar magnitudes, converting magnitudes to fluxes, summing the fluxes, and finally converting back to a combined system magnitude. The synthetic CMD is further processed by adding realistic observational noise sampled from the ASTs (which also accounts for completeness) and applying quality cuts based on the upper magnitude limit and color ranges.

We assume Boo I hosts a single old stellar population formed in a short burst around 13.3 Gyr ([T. M. Brown et al. 2014](#)), with a heliocentric distance of  $d = 65$  kpc (corresponding to a distance modulus of  $m - M = 19.1$ ; [S. Okamoto et al. 2012](#)) and extinction  $A_V = 0.049$  from the [D. J. Schlegel et al. \(1998\)](#) dust map. The metallicities are drawn from the Keck/DEIMOS spectroscopic metallicity distribution function ([M. Geha et al. 2026](#)), peaking at  $[\text{Fe}/\text{H}] = -2.4$  and held fixed during fitting (See Appendix C for more details).

#### 4.2. Empirical Calibrations for Stellar Population Modeling

To ensure accurate comparison between our observed CMD and synthetic stellar populations, we ap-

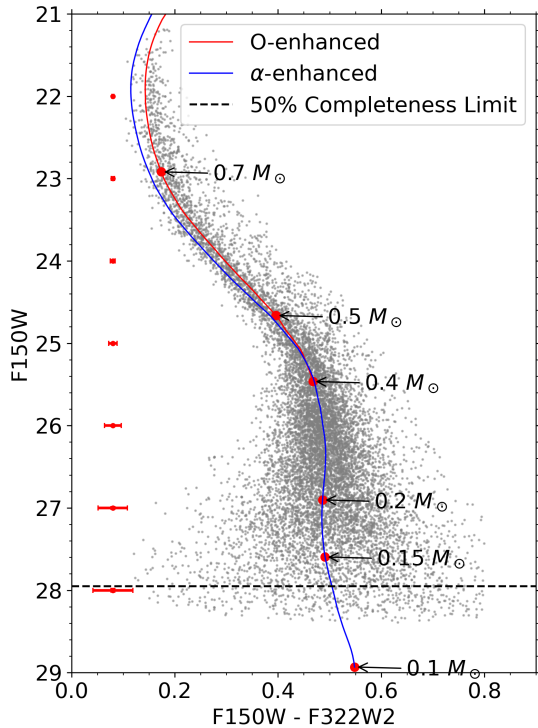


**Figure 4.** CMD of Boo I main-sequence member stars, overlaid with BaSTI  $\alpha$ -enhanced isochrone (blue) and our O-enhanced isochrone (red), both having an age of 13.3 Gyr and  $[\text{Fe}/\text{H}] = -2.4$ , with labels indicating specific stellar masses. The red error bars indicate the typical photometric uncertainties at each magnitude.

ply two critical empirical calibrations: (1) a magnitude-dependent color correction to account for systematic offsets between observed CMD and theoretical isochrones, and (2) additional photometric scatter to match the intrinsic uncertainties present in the observational data. With the synthetic CMD simulator, we generate a fiducial synthetic CMD following the literature log-normal IMF parameters from *C. Filion et al. (2022)* and compare it with the observed CMD to correct for the underlying discrepancy between our model and data empirically.

#### 4.2.1. Model-Data Color Correction

Despite using the stellar model that accounts for high oxygen abundance as detailed in Section 3, we still observe a small but non-negligible magnitude-dependent color shift between the fiducial synthetic and observed CMDs. For both the observed and synthetic CMDs, we compute robust ridge lines by dividing the data into magnitude bins with width=0.3 mag spanning the F150W magnitudes from 21 to 28 mag. Within each magnitude bin, we calculate the median color after ap-

plying a  $3\sigma$  clipping to remove outliers. We then determine the correction at each magnitude bin by applying a Gaussian Kernel Density Estimation to the color distribution, finding the color with the maximum probability, and computing the difference between the observed and synthetic ridge lines. To construct a smooth, continuous correction function, we fitted a univariate spline to the measured offsets using the `scipy.interpolate.UnivariateSpline` function. We extended the correction to fainter magnitudes (27–28.5 mag) by forcing the offset to approach zero, preventing unphysical extrapolation at the faint limit, as shown in Figure 5. This empirical correction typically resulted in shifts ranging from 0 to 0.01 mag across the magnitude range, with the largest corrections applied at the turn-off, where systematic differences are most pronounced. After applying this correction, the synthetic and observed ridge lines agreed to within 0.005 mag across the full magnitude range.

#### 4.2.2. Additional Photometric Scatter

The photometric uncertainties in our ASTs do not fully capture the observational uncertainties, as the artificial stars are produced assuming an idealized PSF. To ensure our synthetic populations accurately reproduce the full scatter present in the data, we add magnitude-dependent extra noise to the AST.

We quantify the excess scatter by measuring the width of the color distribution perpendicular to the ridge line for both observed and corrected synthetic CMDs, assuming that the synthetic CMDs captured the physical spread in color from spreads in metallicities, ages, and binary fractions. For magnitude bins of width 0.5 mag from 21 to 28 mag, we compute the perpendicular color residual by subtracting the ridge-line color at each star’s magnitude. To account for the asymmetric nature of the color distribution (particularly the right side affected by unresolved binaries), we measure the color dispersion with only the left-side scatter as the difference between the 50th and 16th percentiles. The extra scatter required to match the observations is computed in quadrature:

$$\sigma_{\text{extra}}(m) = \sqrt{\max(0, \sigma_{\text{AST}}^2(m) - \sigma_{\text{sim}}^2(m))}$$

where  $\sigma_{\text{AST}}$  and  $\sigma_{\text{sim}}$  are the ASTs and synthetic color dispersions, respectively, with the maximum constraint preventing negative variance. We fit a smooth univariate spline to  $\sigma_{\text{extra}}(m)$  to obtain a continuous function of magnitude.

To apply this extra scatter to the ASTs catalog while preserving correlated errors between bands, we used the correlation coefficient  $\rho(m)$  between photometric errors

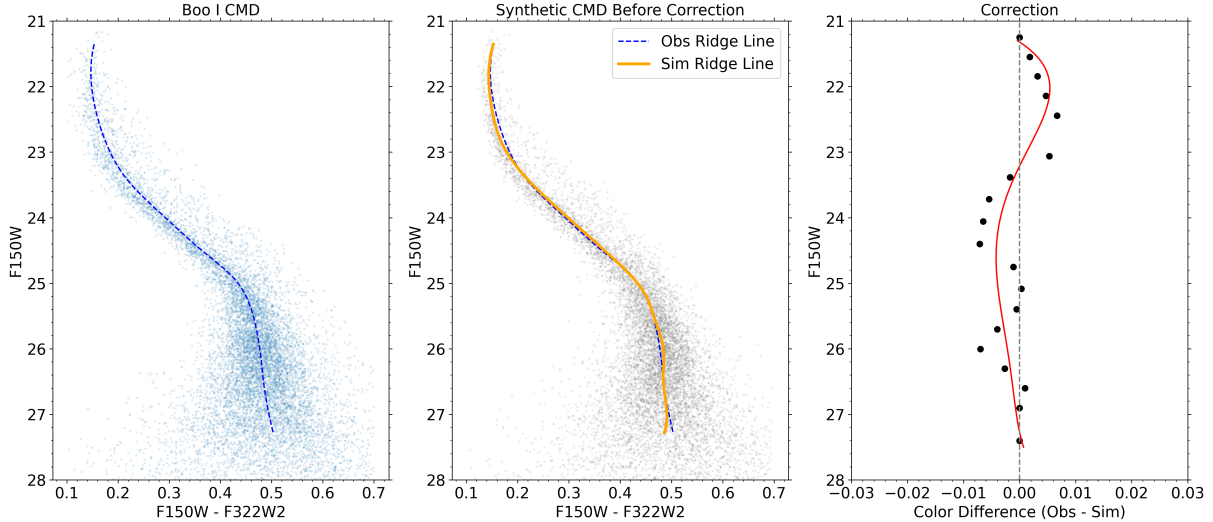


**Figure 5.** Empirical model-data color correction. Left: Observed CMD with ridge line. Middle: Observed (blue) vs. uncorrected synthetic (red) ridge lines reveal systematic color offset. Right: Magnitude-dependent color correction derived from the ridge line difference.

in F150W and F322W2, measured directly from the original ASTs data in each magnitude bin. For each star in magnitude bin  $i$ , we added correlated Gaussian noise drawn from a bivariate normal distribution:

$$\begin{pmatrix} \delta m_{F150W} \\ \delta m_{F322W2} \end{pmatrix} \sim \mathcal{N} \left( \begin{pmatrix} 0 \\ 0 \end{pmatrix}, \begin{pmatrix} \sigma_c^2 & \rho\sigma_c^2 \\ \rho\sigma_c^2 & \sigma_c^2 \end{pmatrix} \right)$$

where the per-band noise amplitude is:

$$\sigma_c = \sigma_{\text{extra}} / \sqrt{2(1 - \rho)} \quad (3)$$

The measured extra scatter ranged from approximately 0.015 mag at bright magnitudes to 0.035 mag at fainter magnitudes, with correlation coefficients  $\rho$  typically between 0.3 and 0.6. After applying both the empirical color correction and the extra scatter, our synthetic CMDs accurately reproduced both the shape and width of the observed CMD across the full magnitude range. These calibrations are applied consistently to all synthetic stellar populations used in our inference framework, ensuring robust constraints on the stellar mass function and other population parameters.

#### 4.3. Simulation-based Inference

We use SBI Sequential Neural Posterior Estimation (SNPE; G. Papamakarios & I. Murray 2016; J.-M. Lueckmann et al. 2017; D. S. Greenberg et al. 2019) to perform Bayesian parameter estimation for our model, where the likelihood is intractable. This approach trains a neural network to directly approximate the posterior distribution by learning from model simulations, enabling efficient inference from observed data. Here we present a high-level overview of the method:

- (i) Initial Simulation Round: Draw parameter vectors  $\theta_i \sim p(\theta)$  from the prior distribution and generate corresponding simulated data  $x_i \sim p(x|\theta_i)$  using the forward model. This produces an initial training dataset  $\mathcal{D}_0 = (\theta_i, x_i)$ . In our context,  $\theta$  denotes the stellar population parameters (e.g., IMF parameters, age, or metallicity), and  $x$  corresponds to the synthetic CMD generated by the population synthesis model.
- (ii) Density Estimation: Train a conditional neural density estimator  $q_\phi(\theta|x)$  to approximate the posterior distribution  $p(\theta|x)$  given samples from  $\mathcal{D}_0$ . The estimator is optimized to minimize the negative log-likelihood  $\mathbb{L}(\theta, x) \sim -\log q_\phi(\theta|x)$ .
- (iii) Sequential Refinement: Condition the trained model on the observed data  $x_{\text{obs}}$  to obtain an approximate posterior  $q_\phi(\theta|x_{\text{obs}})$ . Use this distribution as the proposal distribution  $p_{\text{prop}}(\theta)$  for subsequent simulations, generating new samples  $\theta_i \sim p_{\text{prop}}(\theta)$  and  $x_i \sim p(x|\theta_i)$ . The newly simulated dataset  $\mathcal{D}_t$  is then combined with or replaces previous rounds to retrain  $q_\phi(\theta|x)$ , progressively refining the posterior in regions of high posterior density.
- (iv) Inference: After several rounds, the final density estimator  $q_\phi(\theta|x_{\text{obs}})$  provides a tractable and differentiable approximation to the true posterior  $p(\theta|x_{\text{obs}})$ , enabling efficient posterior sampling and uncertainty quantification without further simulations.

#### 4.4. Kernel Approximation

The SNPE algorithm requires a fixed-length, numerical summary of the observable that is permutation-invariant and captures the data distribution; however, in our case, the number of stars in a CMD is not fixed and the stellar entries are unordered. Therefore, we need a kernel approximation that projects the CMD data points into a high-dimensional feature vector.

We first Min-Max scale each CMD so that color and magnitude contribute comparably. Then each star  $x$  is mapped into the reproducing kernel Hilbert space  $\mathcal{H}$  associated with the radial basis function (RBF) kernel:

$$k(x, y) = \exp(-\gamma|x - y|^2) \quad (4)$$

The  $\gamma$  controls the kernel bandwidth (equivalently  $\gamma = 1/(2\sigma^2)$  in which  $\sigma$  is the Gaussian width). The RBF is a smooth, shift-invariant similarity: nearby points map to values  $\approx 1$  and distant points map to values  $\approx 0$ , so it captures local clustering and continuous structure in CMD space. The choice of  $\gamma$  determines the scale of “nearness”: small  $\gamma$  (large  $\sigma$ ) produces a very broad kernel that treats many points as similar, emphasizing global structure but smoothing out small-scale features, such as the equal-mass binary sequence; on the other hand, large  $\gamma$  (small  $\sigma$ ) makes the kernel very local and sensitive to fine, small-scale differences.

While the kernel is defined on individual stars, our goal is to compare entire CMDs (i.e., sets of stars). We therefore map each catalog to a single representation using a kernel mean embedding, defined as the average of the feature maps of its constituent stars. The RBF kernel corresponds to an implicit mapping into a reproducing kernel Hilbert space  $\mathcal{H}$ , with  $k(x, y) = \langle \phi(x), \phi(y) \rangle_{\mathcal{H}}$ . Under this construction, a CMD  $\{x_i\}$  is represented by  $\mu = \frac{1}{N} \sum_i \phi(x_i)$ , so that distances between CMDs correspond to Euclidean distances between their embeddings in  $\mathcal{H}$ . In the original space, these distances are equivalent to sums of pairwise kernel evaluations across all stars in the two catalogs.

The feature map  $\phi(x)$  is infinite-dimensional, making direct computation infeasible. We therefore approximate it using the Nyström method (C. Williams & M. Seeger 2000), which selects a set of  $n$  landmark points and constructs a low-rank feature map  $\phi_{\text{Nys}}(x) \in \mathbb{R}^n$  such that

$$k(x, y) \approx \phi_{\text{Nys}}(x)^\top \phi_{\text{Nys}}(y).$$

This does not explicitly compute the true infinite-dimensional mapping, but instead provides a finite-dimensional representation whose inner products approximate the kernel. The per-star feature vectors  $\phi_{\text{Nys}}(x_i)$  are then aggregated across the catalog to form

a permutation-invariant embedding  $\mu \in \mathbb{R}^n$ . In this approximation, distances between CMDs reduce to standard Euclidean distances in  $\mathbb{R}^n$ , providing an efficient surrogate for the full kernel-based comparison.

This Nyström+RBF pipeline therefore provides a compact, nonlinear, permutation-invariant summary of CMDs that captures both their global distribution and local geometric structure at scales set by  $\gamma$ , while remaining computationally efficient. The key hyperparameters are  $\gamma$  (kernel width) and  $n$  (number of landmark points), which jointly control the trade-off between sensitivity to fine CMD features, approximation accuracy, and runtime. To determine the optimal hyperparameters and quantify the intrinsic uncertainty of our method, we perform convergence tests that recover known input parameters (Appendix D).

#### 4.5. Parameters and Priors

Using the SBI framework, **Starwave** simultaneously fits high-dimensional stellar population parameters by sampling from their joint distributions. We fit three different IMF parameterizations, including a single power law (SPL),

$$p_{\text{SPL}}(m|\alpha) \propto m^\alpha \quad (5)$$

a broken power law (BPL),

$$p_{\text{BPL}}(m|\alpha_{\text{high}}, \alpha_{\text{low}}, M_b) \propto \begin{cases} m^{\alpha_{\text{high}}} & m > M_b \\ km^{\alpha_{\text{low}}} & m < M_b \end{cases}$$

$$k = M_b^{\alpha_{\text{high}} - \alpha_{\text{low}}} \quad (6)$$

and a log-normal function (LN)

$$p_{\text{LN}}(m|M_c, \sigma) \propto \frac{1}{m} e^{-\frac{1}{2} \left( \frac{\log m - \log(M_c)}{\sigma} \right)^2} \quad (7)$$

The IMF parameters are also degenerate with the number of stars and the binary fraction, which we include as model parameters. We model the total number of stars as a Poisson distribution with intensity  $\log N_{\text{tot}}$ , and treat  $\log N_{\text{tot}}$  as a free parameter with a uniform prior from 2 to 6. The binary fraction  $f(\text{bin})$  has a uniform prior from 0 to 1, corresponding to the range from no binary stars to all binary stars, and we assume a constant binary fraction for all system masses and mass ratios. By combining these parameters, our model samples their joint distribution, encompassing both the stellar population ( $[\log N_{\text{tot}}, f(\text{bin})]$ ) and the IMF parameters. In Appendix E, we also explore the degeneracy of the IMF parameters with the physical stellar population parameters.

## 5. RESULTS

With the photometry, artificial star tests, and the stellar models, we use *Starwave* to conduct the Bayesian inference of the IMF parameters. We run the inference for 5 rounds with 3000 simulations per round, and we sample the joint distribution of the parameters from the last round as our final posterior.

The joint distribution of the best-fit parameters as shown in Figure 6a, 6b, 6c for the SPL, BPL, LN models, respectively. In each plot, the red line indicates the canonical reference value of the IMF parameters from the solar neighborhood (E. E. Salpeter 1955; P. Kroupa 2001; G. Chabrier 2003). In Table 2, we present the median as well as the 68%, 95%, and 99% confidence intervals (CI) of the marginal distributions of the posteriors.

### 5.1. Comparison to the Canonical MW Models

We find our best-fit single power-law slope to be  $\alpha = -1.60_{-0.04}^{+0.04}$ , which is inconsistent with the E. E. Salpeter (1955) slope of  $\alpha = -2.35$  at a 99% confidence level. However, we note that a single power-law model is not a valid description of the very low mass IMF due to its diverging nature, and the canonical Salpeter IMF was derived from a sample with very limited depth. As analyzed in K. El-Badry et al. (2017), if the true underlying IMF follows a log-normal, fitting an SPL over an extended low-mass range leads to an artificially shallower inferred slope as the observation gets deeper. Since our analysis reaches well below the characteristic mass or inflection point identified by P. Kroupa (2001) (and the flattening mass in G. Chabrier 2003), it is therefore unsurprising that the SPL model fails to capture the IMF shape and yields a slope inconsistent with E. E. Salpeter (1955). A similar trend is evident in our later comparison with results from other literature analyses of varying depth.

Our best-fit broken power-law parameters are  $\alpha_{low} = -1.31_{-0.07}^{+0.07}$  below the break mass,  $\alpha_{high} = -1.99_{-0.22}^{+0.16}$  above the break mass, and the break point following  $M_b = 0.47_{-0.07}^{+0.09} M_{\odot}$ . We apply a relatively narrow range to the prior for the break mass, from  $0.35 M_{\odot}$  to  $0.65 M_{\odot}$ , because our data span only a small mass range and provide only weak constraints on the break mass. Since our goal is to test whether a broken power law provides a better description of the data than a single power law, we require the break mass to lie near the center of the observed mass range. Allowing the break mass to vary over a broader range, comparable to or larger than the observed mass range, would cause the sampler to push it toward the boundaries of the data if the sampler and machine learning model exhibit potential underlying bias or

overfitting. In that case, the model effectively reduces to a single power law, leaving the second slope poorly constrained.

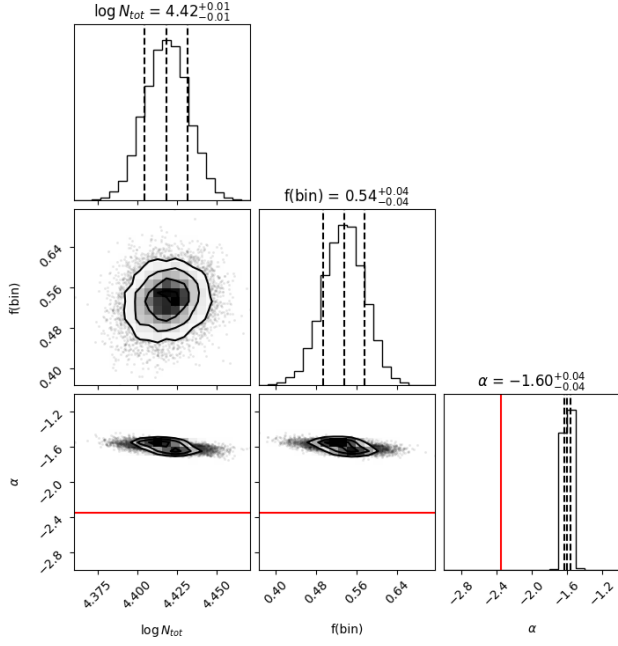
The best-fitting log-normal parameters are a characteristic mass  $M_c = 0.18_{-0.02}^{+0.02} M_{\odot}$  and a width  $\sigma = 0.56_{-0.06}^{+0.06}$ . As the relative uncertainties reach  $\sim 10\%$ , the result provides strong evidence that the Boo I log-normal IMF is consistent with the G. Chabrier (2003) values of  $M_c = 0.2 M_{\odot}$  and  $\sigma = 0.55$  within the 68% confidence interval.

Single Power Law				
Parameter	Median	68% CI	95% CI	99% CI
$\log N_{tot}$	4.42	+0.01 -0.01	+0.03 -0.03	+0.04 -0.04
f(bin)	0.54	+0.04 -0.04	+0.08 -0.08	+0.12 -0.13
$\alpha$	-1.60	+0.04 -0.04	+0.07 -0.07	+0.11 -0.11
Broken Power Law				
Parameter	Median	68% CI	95% CI	99% CI
$\log N_{tot}$	4.38	+0.03 -0.02	+0.05 -0.05	+0.08 -0.08
f(bin)	0.60	+0.08 -0.08	+0.15 -0.15	+0.23 -0.24
$\alpha_{low}$	-1.31	+0.07 -0.07	+0.14 -0.13	+0.21 -0.19
$\alpha_{high}$	-1.99	+0.16 -0.22	+0.27 -0.50	+0.38 -0.77
$M_b$	0.47	+0.09 -0.07	+0.15 -0.11	+0.17 -0.12
Log Normal				
Parameter	Median	68% CI	95% CI	99% CI
$\log N_{tot}$	4.35	+0.05 -0.05	+0.10 -0.10	+0.15 -0.15
f(bin)	0.51	+0.03 -0.03	+0.07 -0.06	+0.12 -0.09
$M_c$	0.18	+0.02 -0.02	+0.05 -0.05	+0.07 -0.07
$\sigma$	0.56	+0.06 -0.06	+0.13 -0.11	+0.21 -0.17

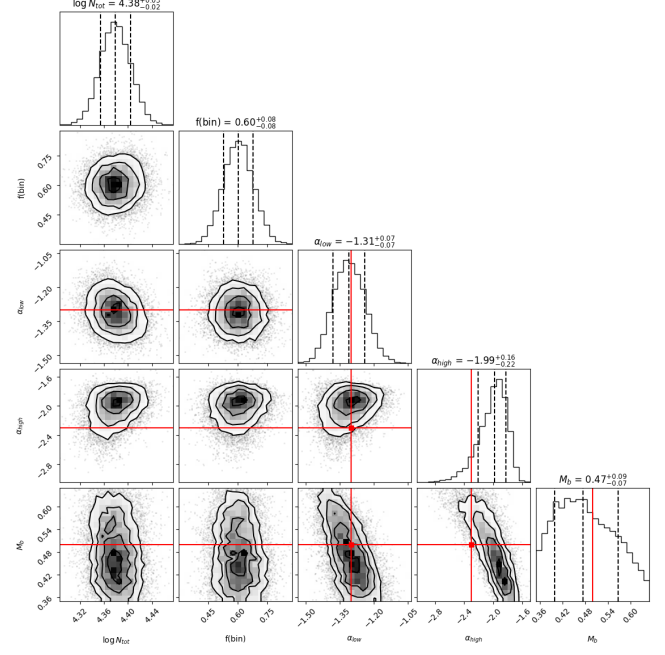
**Table 2.** Posterior parameter estimates for all three IMF models, together with the 68%, 95%, and 99% confidence interval (CI) of the marginal posterior distributions.

### 5.2. Goodness-of-Fit

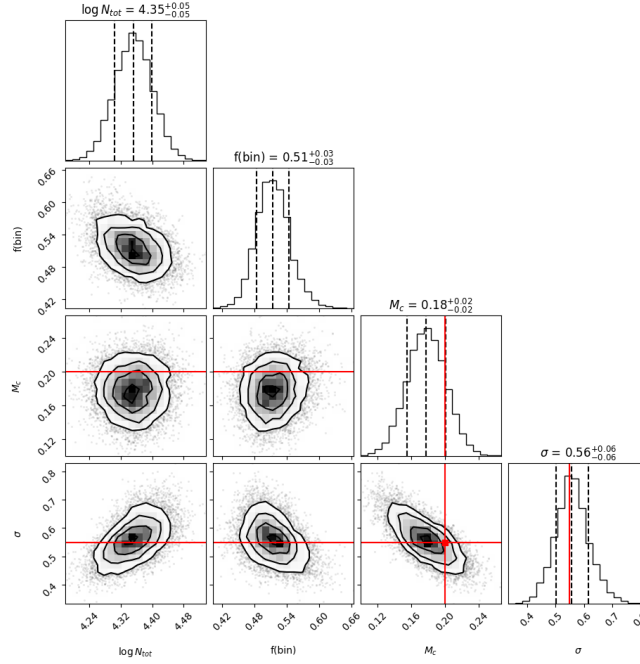
To qualitatively assess the goodness-of-fit, we draw 1000 samples from the posterior for each model and use them to simulate CMDs. From these simulations, we



(a) SPL model. The reference slope  $\alpha = -2.35$  (E. E. Salpeter 1955) is shown in red.



(b) BPL model. Reference values  $\alpha_{\text{low}} = -1.3$ ,  $\alpha_{\text{high}} = -2.3$ ,  $M_b = 0.5M_{\odot}$  (P. Kroupa 2001) are shown in red.



(c) LN model. Reference values  $M_c = 0.2M_{\odot}$ ,  $\sigma = 0.55$  (G. Chabrier 2003) are shown in red.

**Figure 6.** Corner plots of the posterior distributions for the three IMF models, and the conditional posterior of the BPL model with  $M_b \in 0.5 \pm 0.05$ . Vertical dashed lines indicate the 16th, 50th, and 84th percentiles of the marginal distributions. Red lines denote reference measurements from the solar neighborhood.

compute cumulative luminosity functions in the F150W band and compare them to the luminosity function of the observed CMD; the comparison is presented in Figure 7. Overall, the simulated data based on the BPL and LN posteriors show good agreement with the observations. In contrast, the SPL model predicts a comparatively more bottom-light IMF, leading to a poorer match to the observed luminosity function.

We also visually inspect the fit by comparing the observed and posterior CMDs. From the posterior distribution, we generate 1000 sampled CMDs and concatenate them into a single combined CMD. We then randomly draw 0.1% of the combined entries to construct a representative CMD that captures the underlying multi-dimensional parameter distribution. Next, we construct two-dimensional histograms for both the observed CMD and the posterior-sampled CMD. To quantify their difference, we define the significance as

$$S = \frac{N_{obs} - N_{pos}}{\sqrt{N_{obs}}} \quad (8)$$

which represents the normalized difference in star counts between the posterior and observed CMDs in each bin, assuming Poisson noise. In Figure 8, the top-left panel presents the two-dimensional histogram of the observed CMD, and the remaining three panels show the corresponding significance distributions for each model. Since the adopted bin size is comparable to or smaller than the photometric uncertainty, individual bins are not expected to match exactly; however, the overall agreement between the model and observed CMDs remains reasonable.

To derive a more quantitative assessment of the goodness-of-fit and see whether the model predictions are consistent with our observed data, we use a goodness-of-fit criterion defined in M. Gennaro et al. (2018b), which is based on L. Lemaire et al. (2016) with the following steps:

- (i) Randomly draw two subsets of the posterior CMDs, a training set  $\{x_j\}_{j \in J}$ , and a testing set  $\{x_k\}_{k \in K}$
- (ii) Compute, for each  $k \in K$ , the average distance between the CMD  $x_k$  and all CMDs in the training set:

$$\mathcal{D}_{post,k} = \frac{1}{N_j} \sum_{j \in J} \langle \phi(x_j), \phi(x_k) \rangle_{\mathcal{H}} \quad (9)$$

in which  $\langle \phi(x_j), \phi(x_k) \rangle_{\mathcal{H}}$  is the lifted distance between two CMDs in the kernel space as defined in Section 4.4.

- (iii) Compute the average distance between the training set and the observed CMD:

$$\mathcal{D}_{post,obs} = \frac{1}{N_j} \sum_{j \in J} \langle \phi(x_{obs}), \phi(x_k) \rangle_{\mathcal{H}} \quad (10)$$

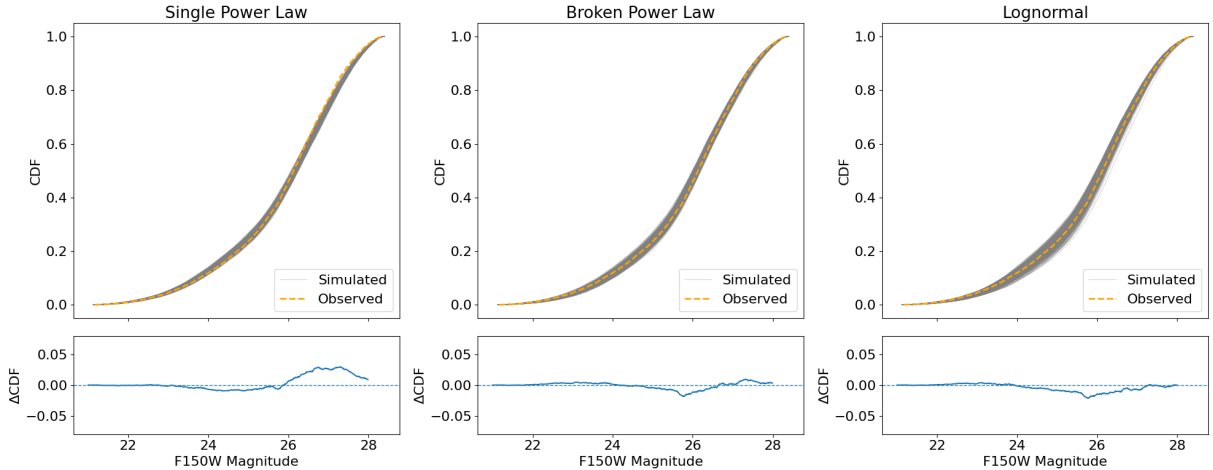
- (iv) Compare  $\mathcal{D}_{post,obs}$  with the distribution of  $\mathcal{D}_{post,k}$  and see if it falls outside some pre-defined quantile.

Figure 9 presents the results of the goodness-of-fit analysis for the three IMF models. The BPL and LN models show strong agreement with the observations, with consistency tighter than the 68% confidence level, whereas the SPL model is disfavored and can be ruled out at the 68% confidence level. This suggests that a peak mass is necessary to explain the observed luminosity function, whereas a single power-law, characterized by its divergence at the low-mass end, is not sufficient.

## 6. DISCUSSIONS

### 6.1. Comparison to Literature Studies of Boo I IMF

Given its proximity to the MW and its relatively high surface brightness, Boo I has been the subject of multiple studies aimed at constraining the low-mass IMF. M. Gennaro et al. (2018a) analyzed the IMFs of six UFDs, including Boo I, using deep HST/ACS photometry down to  $\sim 0.45M_{\odot}$ . They obtained a best-fit single power-law slope of  $\alpha = -1.84$  and best-fit log-normal parameters of  $M_c = 0.33$  and  $\sigma = 0.59$ . Later, C. Filion et al. (2022) used HST ACS/WFC imaging to probe the IMF down to  $\sim 0.3M_{\odot}$ . Their results include a single power-law slope of  $\alpha = -1.95^{+0.93}_{-1.04}$ , broken power-law slopes of  $\alpha_{low} = -1.67^{+0.48}_{-0.57}$  and  $\alpha_{high} = -2.57^{+0.93}_{-1.04}$ , and log-normal parameters of  $M_c = 0.17^{+0.05}_{-0.11}M_{\odot}$  and  $\sigma = 0.49^{+0.13}_{-0.20}$ . It is worth noting that in M. Gennaro et al. (2018a) and our analysis, we treat binary systems as a single mass and fit the system IMF, while C. Filion et al. (2022) fitted the single-star IMF; thus, the results should not be directly compared numerically. Although previous studies did not reach the IMF peak mass and were therefore subject to large uncertainties, our deeper observations extend to the peak mass and arrive at a consistent qualitative conclusion: when IMF models with a characteristic peak mass (i.e., broken power-law or lognormal forms) are adopted, the Boo I IMF is consistent with that of the MW. In contrast, the single power-law slopes are not statistically consistent, a discrepancy that aligns with the prediction of K. El-Badry et al. (2017) that deeper observations can artificially favor a more bottom-light IMF in the context of the SPL model.



**Figure 7.** Cumulative luminosity function of observed stars (orange dashed line) compared to posterior synthetic CMDs (gray lines). The synthetic samples represent 1000 realizations drawn from the posterior parameter distributions. The lower panels show the corresponding differences in cumulative distribution functions:  $\Delta\text{CDF} = (\text{observed CDF}) - (\text{mean of simulated CDFs})$ .

## 6.2. Comparison to Literature Studies of Extragalactic Targets in the Local Universe

Leveraging the deep imaging capabilities of HST, numerous studies have resolved individual extragalactic stars in the local volume to constrain the stellar IMF and reconstruct the star-formation histories of nearby galaxies (see, e.g., Section 3.1 of the review by [N. Bastian et al. 2010](#)). However, the results vary with the mass range probed; therefore, we compare only our results with previous studies that reach mass limits of  $\lesssim 0.5M_{\odot}$ .

Table 3 summarizes IMF parameters for UFD galaxies inferred from deep HST imaging ([M. Geha et al. 2013](#); [M. Gennaro et al. 2018a,b](#); [C. Filion et al. 2024](#)). We note that these studies adopted different modeling assumptions, including whether certain parameters are fixed during fitting and whether binaries are treated in terms of single-star or system masses, so the results are not directly comparable in a strictly numerical sense. However, some qualitative trends emerge from the comparison. In particular, all studies infer single power-law IMF slopes shallower than the canonical Salpeter value of  $\alpha = -2.35$  ([E. E. Salpeter 1955](#)). The inferred slopes also appear to correlate with observational depth, likely reflecting the increased leverage on the low-mass regime afforded by deeper data rather than an intrinsic variation alone.

For the lognormal model, our result is aligned with the previously suggested trend of decreasing characteristic mass  $M_c$  with increasing  $[\text{Fe}/\text{H}]$ , as illustrated in Figure 10, although the trend is not statistically significant given the current uncertainties. There is the theoretical expectation that the IMF should be bottom-light (high

$M_c$ ) in low  $[\text{Fe}/\text{H}]$  star-forming environments (e.g., [P. Kroupa et al. 2013](#) and references therein), and a similar trend is observed with JWST in the MW ([C. Yasui et al. 2024](#)). In particular, [P. Sharda & M. R. Krumholz \(2022\)](#) proposed a transition from the primordial regime (metal-poor, gas fragmentation dominated by molecular hydrogen cooling) to the modern regime (metal-rich, dust and feedback dominated regime) at  $Z \sim 10^{-2}Z_{\odot}$ , accompanied by a significant shift in the characteristic mass. Given that Boo I lies on the relatively metal-rich end of currently observed UFDs ([T. M. Brown et al. 2014](#); [M. Geha et al. 2026](#)) with  $[\text{Fe}/\text{H}] = -2.4$ , we cannot rule out the possibility that it remains above this transition threshold and therefore retains a MW-like IMF. In contrast, the IMF of more metal-poor UFDs may exhibit a higher characteristic mass. The mass–metallicity relation would make it difficult to obtain large sample sizes in even more metal-poor (and less massive) UFDs than Boo I. Nonetheless, our analysis demonstrates that JWST/NIRCam observations can constrain  $M_c$  with sufficient precision that, for more data points of deeply observed UFDs, it will be possible to statistically discriminate between metallicity-dependent and universal IMF scenarios in the low-metallicity regime.

## 7. CONCLUSIONS

With JWST/NIRCam, we resolved  $\sim 10,000$  member stars of the Boo I UFD reaching  $\lesssim 0.15M_{\odot}$  to probe the low-mass IMF deeper than the canonical MW IMF peak mass. We use the simulation-based inference technique to infer the single power-law, broken power-law, and lognormal IMF models through forward modeling

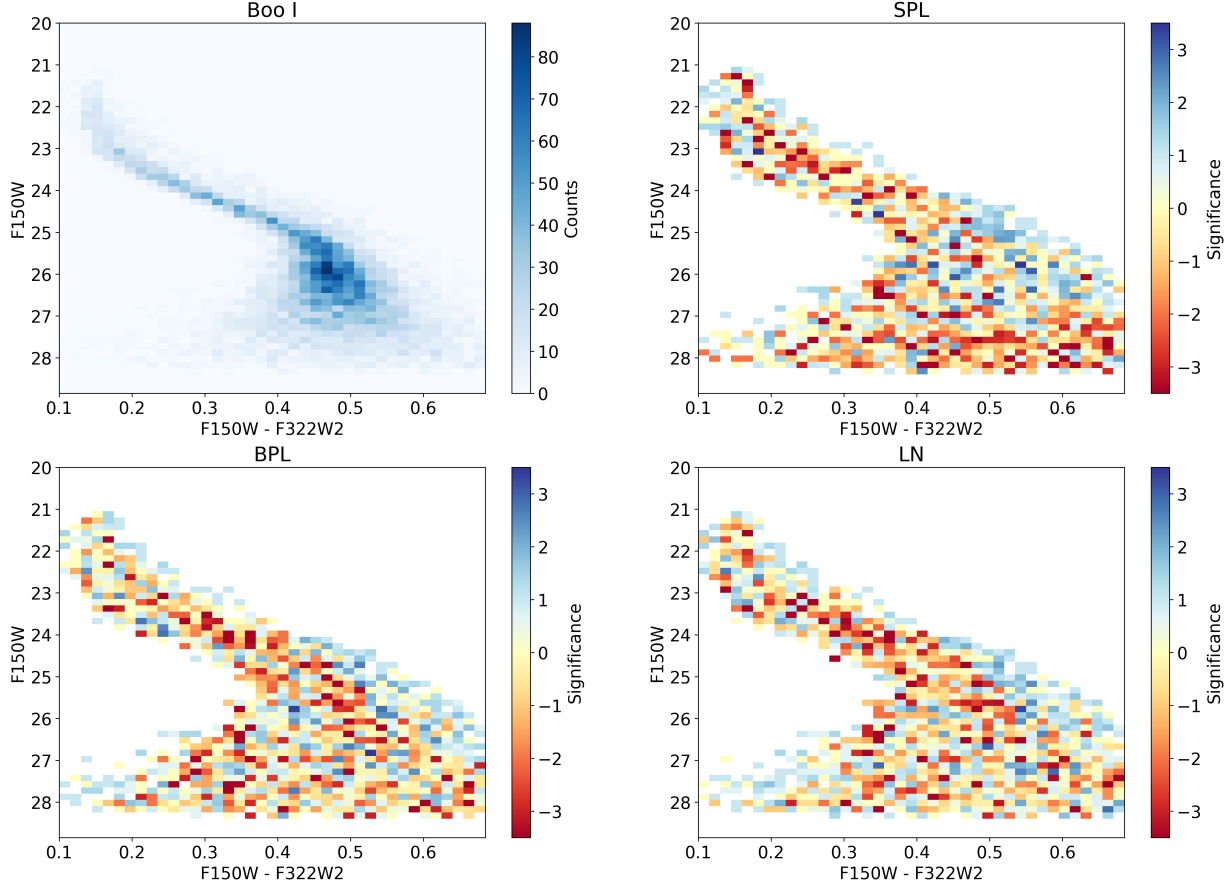


**Figure 8.** Two-dimensional histogram of the observed CMD (top-left panel). The remaining three panels show the corresponding significance maps for each model, as defined in Equation 8. The maps are displayed using a diverging colormap: yellow indicates good agreement, blue regions indicate bins where the observed CMD contains more stars, and red regions indicate bins where the posterior CMD contains more stars.

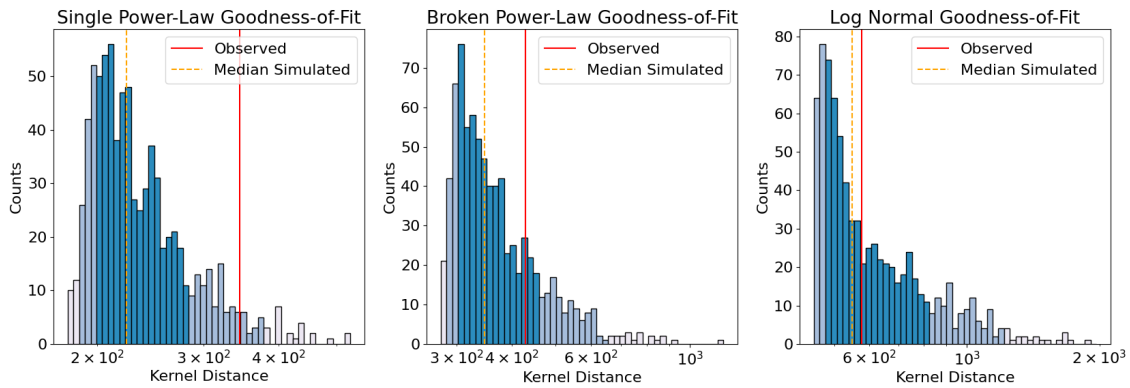


**Figure 9.** Goodness-of-fit measurements for each IMF model. The histogram colors indicate the 68%, 95%, and 99% confidence intervals of  $D_{\text{post},k}$ , with the median marked by the orange dashed line. The red solid line denotes the observed value,  $D_{\text{post,obs}}$ . The SPL model exhibits a substantially larger degree of inconsistency than the other two models.

the stellar population of Boo I and compare the synthetic and observed CMD. Our analysis shows that:

1. The single power-law slope is not consistent with a Salpeter IMF, and the model fails to produce the luminosity function of the observed stars. Through our goodness-of-fit measurement, we can rule out the single power-law model at a 68% confidence level, suggesting that the underlying IMF of Boo I cannot be described by a single power law model, and a peak mass is necessary.
2. The broken power-law model can explain the luminosity function, and the IMF parameters are statistically consistent with those of the MW. The mass break, however, is degenerate with the power-law slopes, which are poorly constrained in our fitting.
3. Our best-fit lognormal IMF is consistent with both the canonical MW IMF and previous Boo I measurements. With our deeper photometry, we probe below the IMF peak mass and reduce the uncertainty on the characteristic mass to 11%, providing further evidence on the invariance of the IMF.

These results provide a window into star formation in the early universe. Under the assumption that Boo I is a local counterpart to a  $\lesssim 10^5 M_\odot$  stellar mass galaxy at  $z \gtrsim 6$  with metallicity down to -2.4, the inferred IMF is consistent with universality across both local and high-redshift environments. This suggests that the characteristic processes governing low-mass star formation may have been established through self-regulation (e.g., P. F. Hopkins et al. 2011; Z. Yan et al. 2023) and remain largely insensitive to variations in the global environment, such as cosmic epoch or modest differences in chemical enrichment.

As our analysis demonstrates the resolving capability of JWST/NIRCam, future observations of UFDs could further confirm or challenge the universality of the IMF. For Boo I, the current observations are effectively near optimal, and deeper imaging is unlikely to be necessary: in the extremely low-mass regime, a narrow stellar-mass interval maps onto a wide luminosity range, so further increasing exposure time would only marginally improve the limiting mass. However, we emphasize that Boo I lies near a favorable balance between distance (and thus effective depth), sky coverage, and available stellar counts. As a result, extending this approach to other UFDs will likely require different observational trade-offs, such as longer exposures for more distant systems (e.g., Hercules), or wider sky coverage for nearer systems (e.g., Coma Berenices).

## 8. ACKNOWLEDGMENTS

This work is based [in part] on observations made with the NASA/ESA/CSA James Webb Space Telescope. The data were obtained from the Mikulski Archive for Space Telescopes at the Space Telescope Science Institute, which is operated by the Association of Universities for Research in Astronomy, Inc., under NASA contract NAS 5-03127 for JWST. These observations are associated with program PID3849.

Support for program PID3849 was provided by NASA through a grant from the Space Telescope Science Institute, which is operated by the Association of Universities for Research in Astronomy, Inc., under NASA contract NAS 5-03127.

*Software:* NumPy (C. R. Harris et al. 2020), SciPy (P. Virtanen et al. 2020), astropy (Astropy Collaboration et al. 2013, 2018, 2022), Matplotlib (J. D. Hunter 2007), sbi (A. Tejero-Cantero et al. 2020), DOLPHOT, (A. E. Dolphin 2000; D. R. Weisz et al. 2024)

*Facility:* JWST

Target	Mass Range ( $M_{\odot}$ )	SPL	BPL	LN	Reference
Hercules	0.52–0.77	$\alpha = -1.2^{+0.4}_{-0.5}$		$M_c = 0.4^{+0.9}_{-0.3}$	M. Geha et al. 2013
	0.45–0.80	$\alpha = -0.93$		$M_c = 0.60$ $\sigma = 0.69$	M. Gennaro et al. 2018a
Leo IV	0.52–0.77	$\alpha = -1.3^{+0.8}_{-0.8}$		$M_c = 0.4^{+2.1}_{-0.3}$	M. Geha et al. 2013
	0.45–0.80	$\alpha = -0.82$		$M_c = 0.62$ $\sigma = 0.69$	M. Gennaro et al. 2018a
Coma Ber	0.45–0.80	$\alpha = -1.66$		$M_c = 0.30$ $\sigma = 0.67$	M. Gennaro et al. 2018a
	0.20–0.75	$\alpha = -1.45^{+0.29}_{-0.30}$	$\alpha_{\text{low}} = -1.18^{+0.49}_{-0.33}$ $\alpha_{\text{high}} = -1.88^{+0.43}_{-0.49}$ $M_b = 0.56^{+0.12}_{-0.12}$	$M_c = 0.33^{+0.16}_{-0.17}$ $\sigma = 0.68^{+0.16}_{-0.12}$	M. Gennaro et al. 2018b
CVn II	0.45–0.80	$\alpha = -1.00$		$M_c = 0.56$ $\sigma = 0.67$	M. Gennaro et al. 2018a
UMa I	0.45–0.80	$\alpha = -1.46$		$M_c = 0.53$ $\sigma = 0.64$	M. Gennaro et al. 2018a
Ret II	0.20–1.00	$\alpha = -1.79^{+0.29}_{-0.27}$	$\alpha_{\text{low}} = -1.77^{+0.40}_{-0.38}$ $\alpha_{\text{high}} = -2.00^{+1.37}_{-1.07}$	$M_c = 0.20^{+0.06}_{-0.15}$ $\sigma = 0.65^{+0.25}_{-0.20}$	C. Filion et al. 2024
UMa II	0.20–1.00	$\alpha = -2.19^{+0.36}_{-0.28}$	$\alpha_{\text{low}} = -2.31^{+0.39}_{-0.36}$ $\alpha_{\text{high}} = -1.60^{+1.52}_{-0.64}$	$M_c = 0.15^{+0.05}_{-0.10}$ $\sigma = 0.53^{+0.13}_{-0.26}$	C. Filion et al. 2024

**Table 3.** Summary of IMF parameters for UFD galaxies derived from deep HST imaging. Uncertainties correspond to the 68% confidence interval when reported. Note that M. Geha et al. (2013) fixed the lognormal  $\sigma$  parameter, while C. Filion et al. (2024) fixed the break mass  $M_b$  in their broken power-law fits.

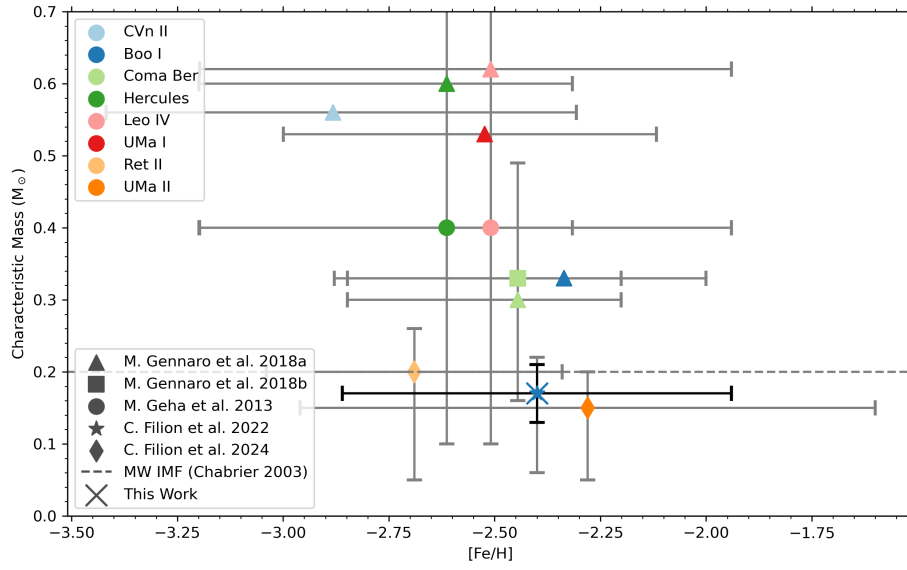


**Figure 10.** Comparison of the best-fit lognormal characteristic mass with literature IMF values as a function of metallicity. The  $[Fe/H]$  represents the values adopted in each study and may vary for the same target. Marker shapes denote the literature sources, while colors represent the target objects. The canonical MW IMF value is shown as a dashed line. There is a mild trend for the characteristic mass to increase with lower  $[Fe/H]$ , though the change is not statistically significant and correlates with the observation depth.

## APPENDIX

## A. EMPIRICAL PHOTOMETRIC QUALITY CUTS

In addition to the fixed photometric quality cuts described in Section 2.3, we apply an empirical data-quality criterion based on magnitude and SNR. For each band, we fit an empirical relation between  $\log(1/\text{SNR})$  and magnitude, and reject sources whose deviation from this relation exceeds 0.2, as shown in Figure 11. This criterion removes extracted sources with photometric uncertainties significantly larger than the typical uncertainty at a given magnitude.

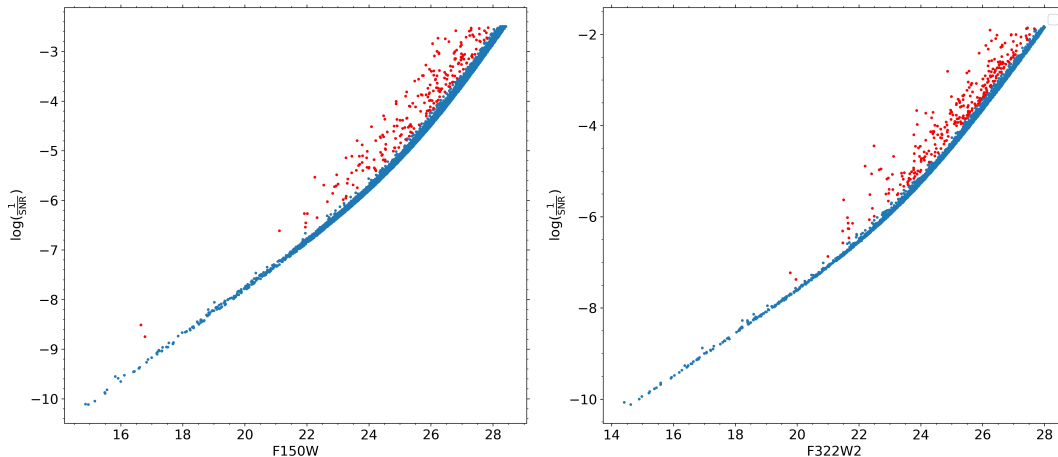


**Figure 11.** Relation between magnitude and  $\log(1/\text{SNR})$  in the F150W (left) and F322W2 (right) bands. The blue points show sources that pass the empirical SNR-based quality cut, while red points indicate rejected sources.

## B. ARTIFICIAL STAR TESTS

As detailed in Section 2.6, the AST input catalog consists of  $10^6$  sources sampled around the Boo I main sequence, together with  $2 \times 10^5$  sources uniformly distributed across the CMD. The left and middle panels of Figure 12 show the luminosity function and CMD of the input catalog, respectively, while the right panel shows the recovered CMD after applying the same photometric quality cuts used for the science catalog. We find that recovery drops sharply beyond  $F150W \gtrsim 28$ , and that the lower main sequence ( $F150W \gtrsim 26$ ) is increasingly broadened by photometric uncertainties.

## C. SPECTROSCOPIC METALLICITY DISTRIBUTION FUNCTION (MDF) OF BOO I

The metallicity distribution function is estimated based on the Keck/DEIMOS spectroscopic  $[\text{Fe}/\text{H}]$  derived in M. Geha et al. (2026). The spectra were reduced with the `PypeIt` pipeline, and the stellar  $[\text{Fe}/\text{H}]$  was determined using the equivalent widths (EWs) of the Ca II triplet (CaT) lines at (8498.0, 8542.1, and 8662.1 Å). M. Geha et al. (2026) also provided the membership probabilities  $P_{mem}$  based on a set of criteria, including metallicity, proper motion, and velocities, and we selected the likely spectroscopic members of Boo I following  $P_{mem} > 0.5$ . To mitigate the effects of binning in the discrete spectroscopic  $[\text{Fe}/\text{H}]$  histogram, we apply the Gaussian Kernel Density Estimation method to interpolate between bins and construct a smooth MDF; the resulting distribution is presented in Figure 13. The resulting MDF is well described by a bell-shaped distribution, peaking at  $[\text{Fe}/\text{H}] = -2.4$  with a standard deviation of 0.46.

## D. SBI HYPERPARAMETER DETERMINATION AND CONVERGENCE TESTS

As discussed in Section 4.4, the SBI includes multiple hyperparameters, such as the number of rounds, the simulations per round, the kernel width, and the dimension for Nyström approximation. Ideally, the number of simulations per round should be as large as possible, but an extremely large number of simulations is unrealistic given that the simulator is hard to parallelize; therefore, we limit our choices to 5 rounds and 3000 simulations per round.

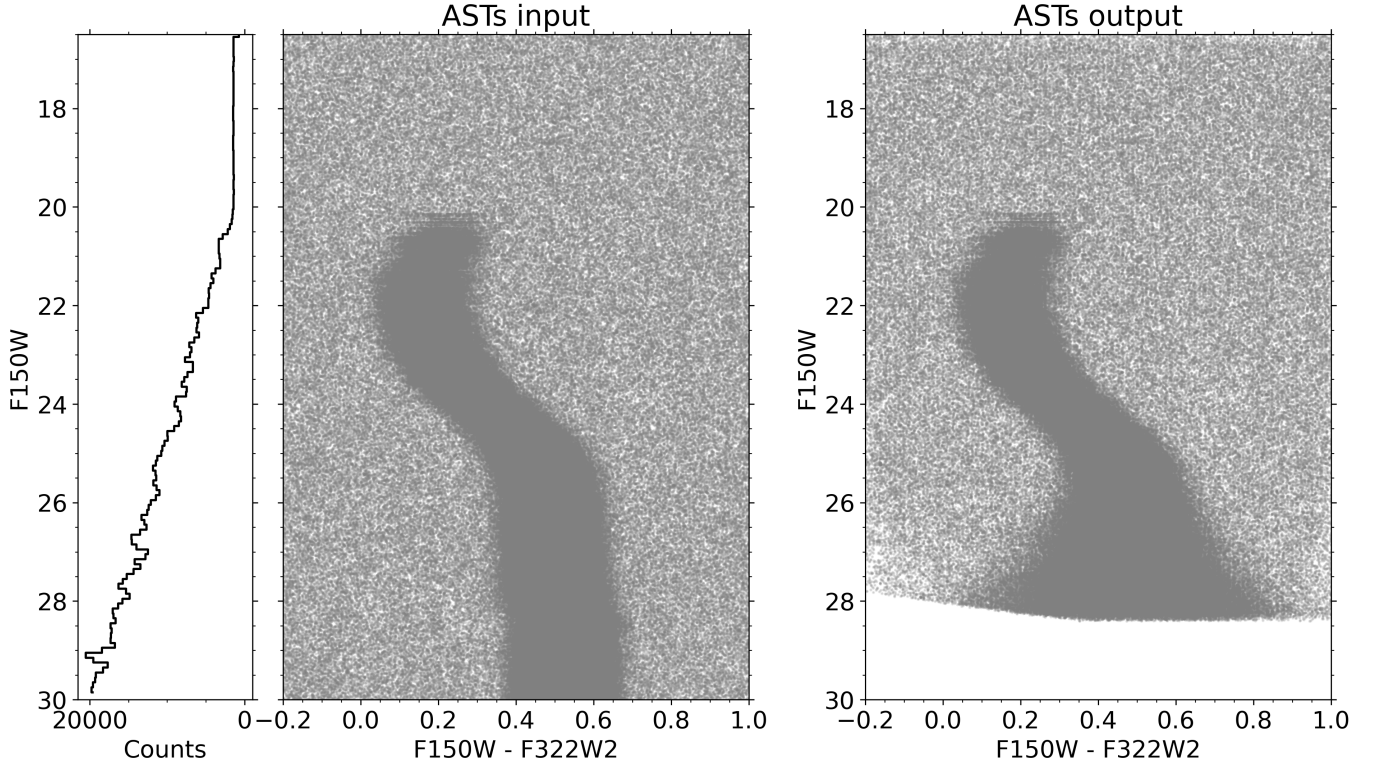


**Figure 12.** Left: the input luminosity function of the artificial stars; Middle: the input CMD used for ASTs; Right: the recovered output CMD from ASTs after applying photometric quality cuts

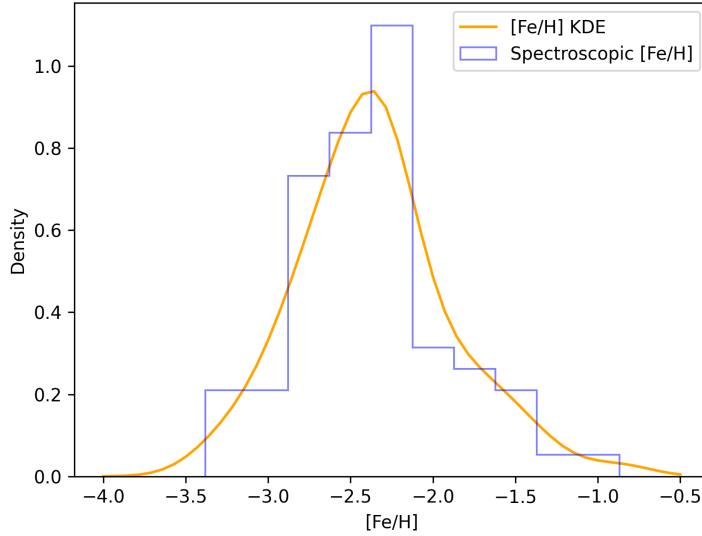


**Figure 13.** The spectroscopic MDF of Boo I, with the blue line showing the [Fe/H] histogram and the orange curve showing the smooth probability density function by smoothing the histogram with a Gaussian Kernel Density Estimation.

With fixed numbers of rounds and simulations, we use the procedure described in Section 4.4 to empirically determine the optimal combination of Gaussian kernel width  $\gamma$  and embedding dimension  $n$ . We first simulate reference CMDs following the physical parameters of Boo I and the canonical MW IMF parameters, incorporating photometric noise

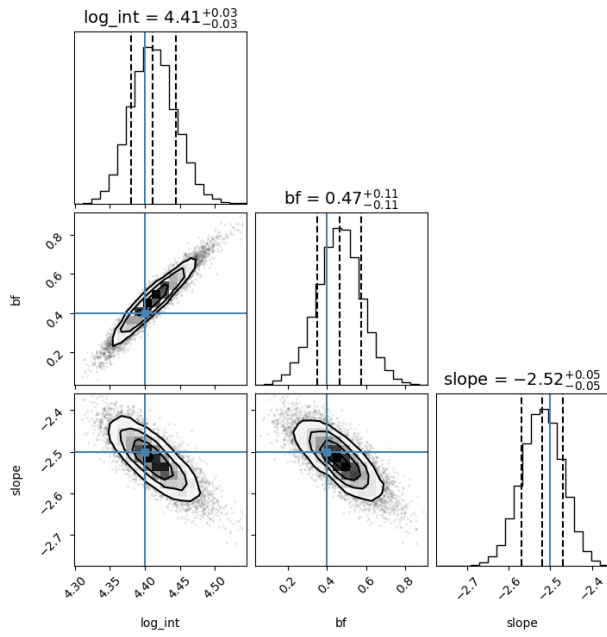
according to our ASTs. We then construct a grid of  $\gamma$  values ranging from 0.5 to 50,000 in steps of  $5 \times 10^k$ , and explore embedding dimensions  $n$  from 25 to 400. Then we feed the reference CMDs back to **Starwave** with each combination of  $\gamma$  and  $n$ , testing whether the method can successfully recover the known input parameters.

The optimal hyperparameter combination is chosen according to two criteria: (1) the parameter uncertainties are minimized while the true values fall within the 68% confidence interval, and (2) the posterior CMDs visually reproduce the luminosity function of the input CMD. Our experiments indicate that  $\gamma = 50$  and  $n = 50$  yield the best overall performance, and the uncertainties in the posteriors can be interpreted as intrinsic uncertainties that cannot be further reduced given our method and data, as demonstrated in Figure 14.

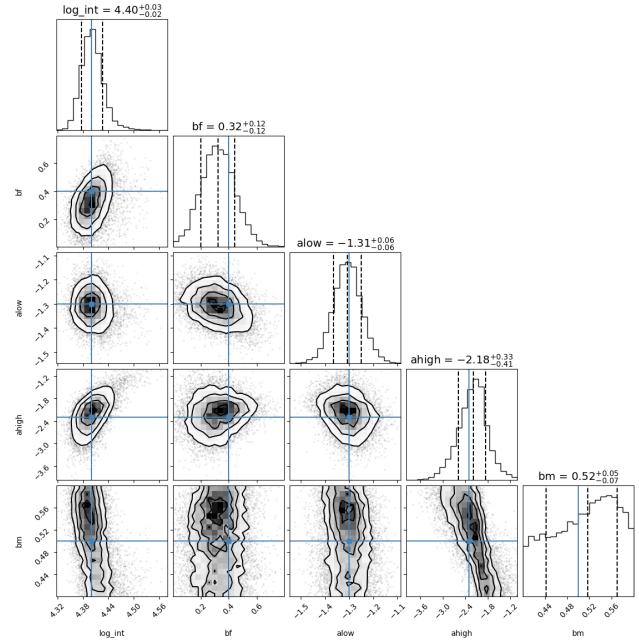
#### E. EFFECTS OF THE STELLAR POPULATION PARAMETERS

To investigate the effect of the physical parameter assumption on the IMF parameters posteriors, to perform another inference in which we allow the stellar population parameters, including binary fraction (bf), distance modulus (dm), extinction (av), and age, to vary, and simultaneously fit these stellar population parameters together with the IMF parameters. It is worth noting here that we keep the [Fe/H] fixed, since we use an empirical MDF distribution that is not parametrized.

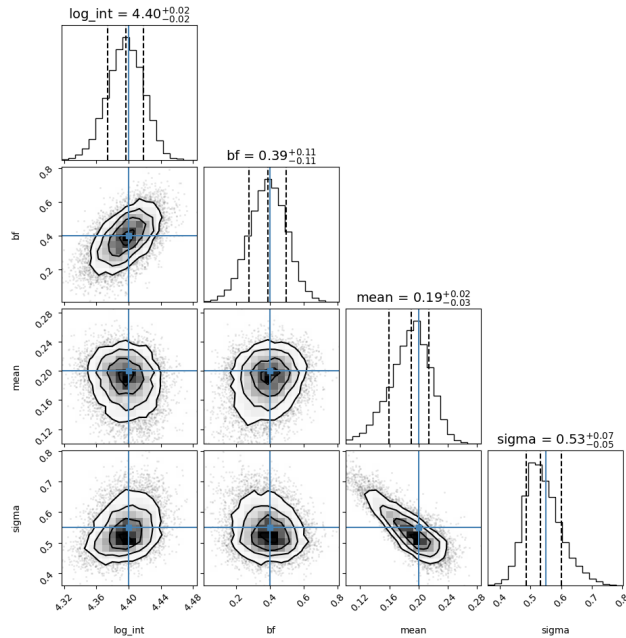
The posterior corner plots are shown in Figure 15. Because our analysis focuses on the nearly vertical part of the main-sequence, the CMD provides only a weak constraint on the binary fraction. In particular, the binary fraction is highly degenerate with the distance modulus, as a higher binary fraction or a lower distance modulus both effectively shift stars to brighter magnitudes on the CMD. The impact of extinction is minimal, as infrared magnitudes are only weakly affected. Moreover, age does not exhibit significant degeneracy with the IMF parameters, since our analysis probes stellar masses below the main-sequence turnoff. Consequently, the assumed stellar population parameters show little correlation with the IMF parameters, and our main conclusions remain robust under modest variations in the adopted physical parameters of Boo I.



(a) Single power-law

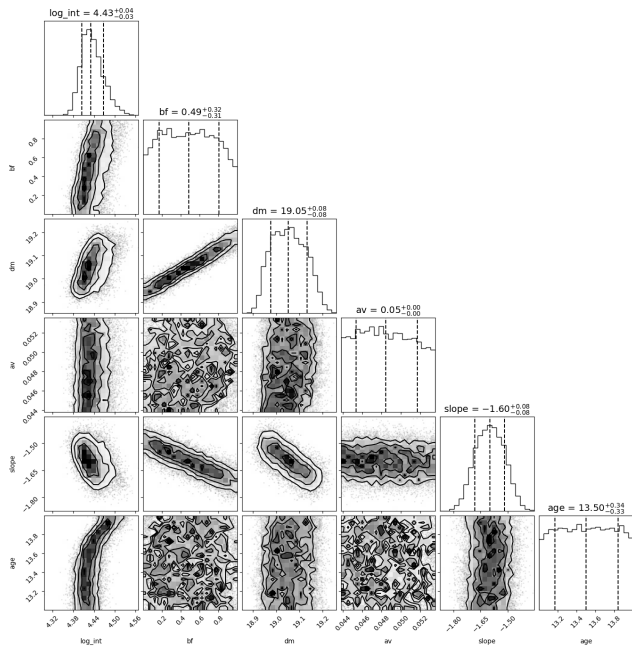


(b) Broken power-law

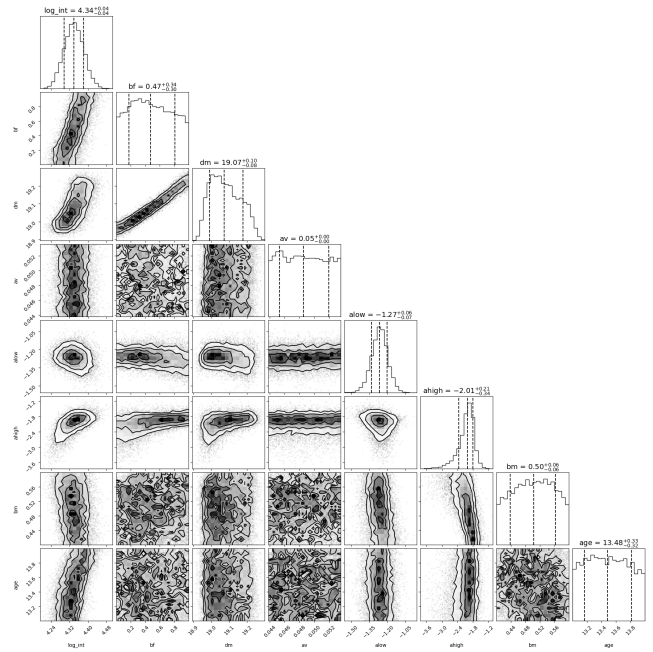


(c) Log-normal

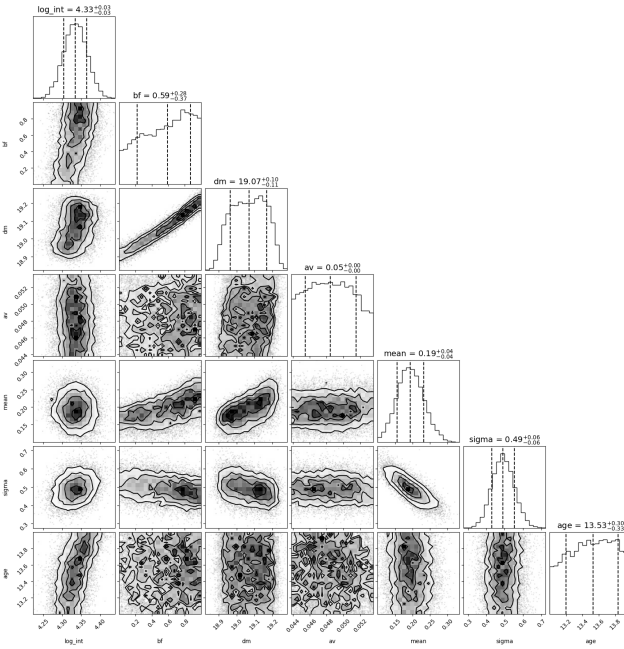
**Figure 14.** Posterior corner plots from the convergence test, with blue lines marking the true (input) parameter values used to generate the reference CMDs.



(a) Single power-law



(b) Broken power-law



(c) Log-normal

**Figure 15.** Corner plots of the posterior distributions for the three IMF models, where the IMF and stellar population parameters are fitted simultaneously. Vertical dashed lines mark the 16th, 50th, and 84th percentiles of the marginal distributions.

## REFERENCES

- Astropy Collaboration, Robitaille, T. P., Tollerud, E. J., et al. 2013, *A&A*, 558, A33, doi: [10.1051/0004-6361/201322068](https://doi.org/10.1051/0004-6361/201322068)
- Astropy Collaboration, Price-Whelan, A. M., Sipőcz, B. M., et al. 2018, *AJ*, 156, 123, doi: [10.3847/1538-3881/aabc4f](https://doi.org/10.3847/1538-3881/aabc4f)
- Astropy Collaboration, Price-Whelan, A. M., Lim, P. L., et al. 2022, *ApJ*, 935, 167, doi: [10.3847/1538-4357/ac7c74](https://doi.org/10.3847/1538-4357/ac7c74)
- Bastian, N., Covey, K. R., & Meyer, M. R. 2010, *ARA&A*, 48, 339, doi: [10.1146/annurev-astro-082708-101642](https://doi.org/10.1146/annurev-astro-082708-101642)
- Bate, M. R. 2014, *MNRAS*, 442, 285, doi: [10.1093/mnras/stu795](https://doi.org/10.1093/mnras/stu795)
- Bate, M. R. 2019, *MNRAS*, 484, 2341, doi: [10.1093/mnras/stz103](https://doi.org/10.1093/mnras/stz103)
- Baumgardt, H., Faller, J., Meinhold, N., McGovern-Greco, C., & Hilker, M. 2022, *MNRAS*, 510, 3531, doi: [10.1093/mnras/stab3629](https://doi.org/10.1093/mnras/stab3629)
- Belokurov, V., Zucker, D. B., Evans, N. W., et al. 2006, *ApJL*, 647, L111, doi: [10.1086/507324](https://doi.org/10.1086/507324)
- Bialy, S., & Sternberg, A. 2019, *ApJ*, 881, 160, doi: [10.3847/1538-4357/ab2fd1](https://doi.org/10.3847/1538-4357/ab2fd1)
- Bovill, M. S., & Ricotti, M. 2009, *ApJ*, 693, 1859, doi: [10.1088/0004-637X/693/2/1859](https://doi.org/10.1088/0004-637X/693/2/1859)
- Bovill, M. S., & Ricotti, M. 2011, *ApJ*, 741, 17, doi: [10.1088/0004-637X/741/1/17](https://doi.org/10.1088/0004-637X/741/1/17)
- Brown, T. M., Tumlinson, J., Geha, M., et al. 2014, *ApJ*, 796, 91, doi: [10.1088/0004-637X/796/2/91](https://doi.org/10.1088/0004-637X/796/2/91)
- Cassisi, S., & Salaris, M. 2020, *A&A Rv*, 28, 5, doi: [10.1007/s00159-020-00127-y](https://doi.org/10.1007/s00159-020-00127-y)
- Chabrier, G. 2003, *PASP*, 115, 763, doi: [10.1086/376392](https://doi.org/10.1086/376392)
- Chandra, V., & Gennaro, M. 2021, in *American Astronomical Society Meeting Abstracts*, Vol. 237, *American Astronomical Society Meeting Abstracts #237*, 329.02
- Cohen, R. E., Gennaro, M., Correnti, M., McQuinn, K. B. W., & Chandra, V. 2026, *ApJ*, 1000, 151, doi: [10.3847/1538-4357/ae4720](https://doi.org/10.3847/1538-4357/ae4720)
- Cranmer, K., Brehmer, J., & Louppe, G. 2020, *Proceedings of the National Academy of Science*, 117, 30055, doi: [10.1073/pnas.1912789117](https://doi.org/10.1073/pnas.1912789117)
- Dolphin, A. 2016, *DOLPHOT: Stellar photometry*, *Astrophysics Source Code Library*, record ascl:1608.013 <http://ascl.net/1608.013>
- Dolphin, A. E. 2000, *PASP*, 112, 1383, doi: [10.1086/316630](https://doi.org/10.1086/316630)
- Durbin, M. J., Choi, Y., Savino, A., et al. 2025, *ApJ*, 992, 106, doi: [10.3847/1538-4357/ae00c8](https://doi.org/10.3847/1538-4357/ae00c8)
- El-Badry, K., Weisz, D. R., & Quataert, E. 2017, *MNRAS*, 468, 319, doi: [10.1093/mnras/stx436](https://doi.org/10.1093/mnras/stx436)
- Filion, C., Platais, I., Wyse, R. F. G., & Kozhurina-Platais, V. 2022, *ApJ*, 939, 38, doi: [10.3847/1538-4357/ac9383](https://doi.org/10.3847/1538-4357/ac9383)
- Filion, C., Wyse, R. F. G., Richstein, H., et al. 2024, *ApJ*, 967, 165, doi: [10.3847/1538-4357/ad4020](https://doi.org/10.3847/1538-4357/ad4020)
- Frebel, A. 2010, *Astronomische Nachrichten*, 331, 474, doi: [10.1002/asna.201011362](https://doi.org/10.1002/asna.201011362)
- Frebel, A., Norris, J. E., Gilmore, G., & Wyse, R. F. G. 2016, *ApJ*, 826, 110, doi: [10.3847/0004-637X/826/2/110](https://doi.org/10.3847/0004-637X/826/2/110)
- Geha, M., Pelliccia, D., Prochaska, J. X., et al. 2026, *arXiv e-prints*, arXiv:2602.10200, doi: [10.48550/arXiv.2602.10200](https://doi.org/10.48550/arXiv.2602.10200)
- Geha, M., Brown, T. M., Tumlinson, J., et al. 2013, *ApJ*, 771, 29, doi: [10.1088/0004-637X/771/1/29](https://doi.org/10.1088/0004-637X/771/1/29)
- Gennaro, M., Ding, K., & Chandra, V. 2026, *starwave*, v0.0 Zenodo, doi: [10.5281/zenodo.19863170](https://doi.org/10.5281/zenodo.19863170)
- Gennaro, M., Tchernyshyov, K., Brown, T. M., et al. 2018a, *ApJ*, 855, 20, doi: [10.3847/1538-4357/aaa973](https://doi.org/10.3847/1538-4357/aaa973)
- Gennaro, M., Geha, M., Tchernyshyov, K., et al. 2018b, *ApJ*, 863, 38, doi: [10.3847/1538-4357/aaceff](https://doi.org/10.3847/1538-4357/aaceff)
- Girardi, L., Barbieri, M., Groenewegen, M. A. T., et al. 2012, in *Astrophysics and Space Science Proceedings*, Vol. 26, *Red Giants as Probes of the Structure and Evolution of the Milky Way*, ed. A. Miglio, J. Montalbán, & A. Noels, 165, doi: [10.1007/978-3-642-18418-5\\_17](https://doi.org/10.1007/978-3-642-18418-5_17)
- Greenberg, D. S., Nonnenmacher, M., & Macke, J. H. 2019, *arXiv e-prints*, arXiv:1905.07488, doi: [10.48550/arXiv.1905.07488](https://doi.org/10.48550/arXiv.1905.07488)
- Gustafsson, B., Edvardsson, B., Eriksson, K., et al. 2008, *A&A*, 486, 951, doi: [10.1051/0004-6361:200809724](https://doi.org/10.1051/0004-6361:200809724)
- Harris, C. R., Millman, K. J., van der Walt, S. J., et al. 2020, *Nature*, 585, 357, doi: [10.1038/s41586-020-2649-2](https://doi.org/10.1038/s41586-020-2649-2)
- Hopkins, P. F., Quataert, E., & Murray, N. 2011, *MNRAS*, 417, 950, doi: [10.1111/j.1365-2966.2011.19306.x](https://doi.org/10.1111/j.1365-2966.2011.19306.x)
- Hunter, J. D. 2007, *Computing in Science & Engineering*, 9, 90, doi: [10.1109/MCSE.2007.55](https://doi.org/10.1109/MCSE.2007.55)
- Kalirai, J. S., Anderson, J., Dotter, A., et al. 2013, *ApJ*, 763, 110, doi: [10.1088/0004-637X/763/2/110](https://doi.org/10.1088/0004-637X/763/2/110)
- Klessen, R. S., & Glover, S. C. O. 2023, *ARA&A*, 61, 65, doi: [10.1146/annurev-astro-071221-053453](https://doi.org/10.1146/annurev-astro-071221-053453)
- Kroupa, P. 2001, *MNRAS*, 322, 231, doi: [10.1046/j.1365-8711.2001.04022.x](https://doi.org/10.1046/j.1365-8711.2001.04022.x)
- Kroupa, P., Weidner, C., Pflamm-Altenburg, J., et al. 2013, in *Planets, Stars and Stellar Systems*. Volume 5: *Galactic Structure and Stellar Populations*, ed. T. D. Oswalt & G. Gilmore, Vol. 5, 115, doi: [10.1007/978-94-007-5612-0\\_4](https://doi.org/10.1007/978-94-007-5612-0_4)
- Legnardi, M. V., Muratore, F., Milone, A. P., et al. 2025, *A&A*, 702, A180, doi: [10.1051/0004-6361/202556239](https://doi.org/10.1051/0004-6361/202556239)
- Lemaire, L., Jay, F., Lee, I.-H., Csilléry, K., & Blum, M. G. B. 2016, *arXiv e-prints*, arXiv:1601.04096, doi: [10.48550/arXiv.1601.04096](https://doi.org/10.48550/arXiv.1601.04096)

- Lueckmann, J.-M., Goncalves, P. J., Bassetto, G., et al. 2017, in *Advances in Neural Information Processing Systems*, ed. I. Guyon, U. V. Luxburg, S. Bengio, H. Wallach, R. Fergus, S. Vishwanathan, & R. Garnett, Vol. 30 (Curran Associates, Inc.).  
[https://proceedings.neurips.cc/paper\\_files/paper/2017/file/addfa9b7e234254d26e9c7f2af1005cb-Paper.pdf](https://proceedings.neurips.cc/paper_files/paper/2017/file/addfa9b7e234254d26e9c7f2af1005cb-Paper.pdf)
- Muñoz, R. R., Côté, P., Santana, F. A., et al. 2018, *ApJ*, 860, 66, doi: [10.3847/1538-4357/aac16b](https://doi.org/10.3847/1538-4357/aac16b)
- Myers, A. T., Krumholz, M. R., Klein, R. I., & McKee, C. F. 2011, *ApJ*, 735, 49, doi: [10.1088/0004-637X/735/1/49](https://doi.org/10.1088/0004-637X/735/1/49)
- Offner, S. S. R., Clark, P. C., Hennebelle, P., et al. 2014, in *Protostars and Planets VI*, ed. H. Beuther, R. S. Klessen, C. P. Dullemond, & T. Henning, 53–75, doi: [10.2458/azu\\_uapress.9780816531240-ch003](https://doi.org/10.2458/azu_uapress.9780816531240-ch003)
- Okamoto, S., Arimoto, N., Yamada, Y., & Onodera, M. 2012, *ApJ*, 744, 96, doi: [10.1088/0004-637X/744/2/96](https://doi.org/10.1088/0004-637X/744/2/96)
- Pacifici, C., Charlot, S., Blaizot, J., & Brinchmann, J. 2012, *MNRAS*, 421, 2002, doi: [10.1111/j.1365-2966.2012.20431.x](https://doi.org/10.1111/j.1365-2966.2012.20431.x)
- Pacifici, C., Kassin, S. A., Weiner, B., Charlot, S., & Gardner, J. P. 2013, *ApJL*, 762, L15, doi: [10.1088/2041-8205/762/1/L15](https://doi.org/10.1088/2041-8205/762/1/L15)
- Papamakarios, G., & Murray, I. 2016, in *Advances in Neural Information Processing Systems*, ed. D. Lee, M. Sugiyama, U. Luxburg, I. Guyon, & R. Garnett, Vol. 29 (Curran Associates, Inc.).  
[https://proceedings.neurips.cc/paper\\_files/paper/2016/file/6aca97005c68f1206823815f66102863-Paper.pdf](https://proceedings.neurips.cc/paper_files/paper/2016/file/6aca97005c68f1206823815f66102863-Paper.pdf)
- Pietrinferni, A., Hidalgo, S., Cassisi, S., et al. 2021, *ApJ*, 908, 102, doi: [10.3847/1538-4357/abd4d5](https://doi.org/10.3847/1538-4357/abd4d5)
- Ricotti, M., & Gnedin, N. Y. 2005, *ApJ*, 629, 259, doi: [10.1086/431415](https://doi.org/10.1086/431415)
- Rocha, M., Peter, A. H. G., & Bullock, J. 2012, *MNRAS*, 425, 231, doi: [10.1111/j.1365-2966.2012.21432.x](https://doi.org/10.1111/j.1365-2966.2012.21432.x)
- Safarzadeh, M., Simon, J. D., & Loeb, A. 2022, *ApJ*, 930, 54, doi: [10.3847/1538-4357/ac626e](https://doi.org/10.3847/1538-4357/ac626e)
- Salpeter, E. E. 1955, *ApJ*, 121, 161, doi: [10.1086/145971](https://doi.org/10.1086/145971)
- Sandford, N. R., Li, T. S., Kaposov, S. E., et al. 2026, *ApJ*, 998, 47, doi: [10.3847/1538-4357/ae2fe5](https://doi.org/10.3847/1538-4357/ae2fe5)
- Schlegel, D. J., Finkbeiner, D. P., & Davis, M. 1998, *ApJ*, 500, 525, doi: [10.1086/305772](https://doi.org/10.1086/305772)
- Sharda, P., & Krumholz, M. R. 2022, *MNRAS*, 509, 1959, doi: [10.1093/mnras/stab2921](https://doi.org/10.1093/mnras/stab2921)
- Shariat, C., El-Badry, K., Gennaro, M., et al. 2025, *PASP*, 137, 104103, doi: [10.1088/1538-3873/ae11d2](https://doi.org/10.1088/1538-3873/ae11d2)
- Sitnova, T. M., Mashonkina, L. I., Tatarnikov, A. M., et al. 2021, *MNRAS*, 504, 1183, doi: [10.1093/mnras/stab786](https://doi.org/10.1093/mnras/stab786)
- STScI Development Team. 2018, synphot: Synthetic photometry using Astropy,, Astrophysics Source Code Library, record ascl:1811.001 <http://ascl.net/1811.001>
- Sunnquist, B., Boyer, M., Brooks, B., et al. 2025, Version 4 of the NIRCcam Wisp Templates: Wisp Characterization, Stability, and Validation Testing, Tech. Rep. Technical Report JWST-STScI-009225, STScI
- Tanvir, T. S., & Krumholz, M. R. 2024, *MNRAS*, 527, 7306, doi: [10.1093/mnras/stad3581](https://doi.org/10.1093/mnras/stad3581)
- Tejero-Cantero, A., Boelts, J., Deistler, M., et al. 2020, *Journal of Open Source Software*, 5, 2505, doi: [10.21105/joss.02505](https://doi.org/10.21105/joss.02505)
- VandenBerg, D. A. 2023, *MNRAS*, 518, 4517, doi: [10.1093/mnras/stac3270](https://doi.org/10.1093/mnras/stac3270)
- VandenBerg, D. A., Bergbusch, P. A., Ferguson, J. W., & Edvardsson, B. 2014, *ApJ*, 794, 72, doi: [10.1088/0004-637X/794/1/72](https://doi.org/10.1088/0004-637X/794/1/72)
- VandenBerg, D. A., Edvardsson, B., Casagrande, L., & Ferguson, J. W. 2022, *MNRAS*, 509, 4189, doi: [10.1093/mnras/stab2996](https://doi.org/10.1093/mnras/stab2996)
- Virtanen, P., Gommers, R., Oliphant, T. E., et al. 2020, *Nature Methods*, 17, 261, doi: [10.1038/s41592-019-0686-2](https://doi.org/10.1038/s41592-019-0686-2)
- Warfield, J. T., Richstein, H., Kallivayalil, N., et al. 2023, *Research Notes of the American Astronomical Society*, 7, 23, doi: [10.3847/2515-5172/acbb72](https://doi.org/10.3847/2515-5172/acbb72)
- Weatherford, N. C., Fragione, G., Kremer, K., et al. 2021, *ApJL*, 907, L25, doi: [10.3847/2041-8213/abd79c](https://doi.org/10.3847/2041-8213/abd79c)
- Weisz, D. R., Dolphin, A. E., Skillman, E. D., et al. 2015, *ApJ*, 804, 136, doi: [10.1088/0004-637X/804/2/136](https://doi.org/10.1088/0004-637X/804/2/136)
- Weisz, D. R., Dolphin, A. E., Savino, A., et al. 2024, *ApJS*, 271, 47, doi: [10.3847/1538-4365/ad2600](https://doi.org/10.3847/1538-4365/ad2600)
- Williams, C., & Seeger, M. 2000, in *Advances in Neural Information Processing Systems*, ed. T. Leen, T. Dietterich, & V. Tresp, Vol. 13 (MIT Press).  
[https://proceedings.neurips.cc/paper\\_files/paper/2000/file/19de10adbaa1b2ee13f77f679fa1483a-Paper.pdf](https://proceedings.neurips.cc/paper_files/paper/2000/file/19de10adbaa1b2ee13f77f679fa1483a-Paper.pdf)
- Wyse, R. F. G., Gilmore, G., Houdashelt, M. L., et al. 2002, *NewA*, 7, 395, doi: [10.1016/S1384-1076\(02\)00156-2](https://doi.org/10.1016/S1384-1076(02)00156-2)
- Yan, Z., Jerabkova, T., & Kroupa, P. 2023, *A&A*, 670, A151, doi: [10.1051/0004-6361/202244919](https://doi.org/10.1051/0004-6361/202244919)
- Yasui, C., Izumi, N., Saito, M., et al. 2024, *ApJ*, 975, 152, doi: [10.3847/1538-4357/ad73a2](https://doi.org/10.3847/1538-4357/ad73a2)